ERDC/GSL TR-04-13

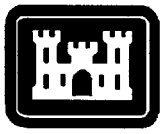

US Army Corps
of Engineers®
Engineer Research and
Development Center

Infrastructure Technologies Research Program

Folsom Dam Outlet Works Modification Project: Dynamic Stress Analysis of Overflow and Nonoverflow Sections

Enrique E. Matheu, Robert L. Hall, and Raju V. Kala

September 2004

Geotechnical and Structures
Laboratory

Infrastructure Technologies Research Program

ERDC/GSL TR-04-13
September 2004

Folsom Dam Outlet Works Modification Project: Dynamic Stress Analysis of Overflow and Nonoverflow Sections

Enrique E. Matheu, Robert L. Hall, and Raju V. Kala

Geotechnical and Structures Laboratory
U.S. Army Engineer Research and Development Center
3909 Halls Ferry Road
Vicksburg, MS 39180-6199

Final report

Prepared for U.S. Army Corps of Engineers
Washington, DC 20314-1000

ABSTRACT:
This report summarizes the results corresponding to a series of dynamic stress analyses performed on an overflow and a nonoverflow monolith of Folsom Dam, California. The monoliths selected for analysis were monoliths 14 and 21, and they were chosen as representative of critical overflow and nonoverflow configurations. The analyses were conducted using the computer program EAGD-84, developed by Professor A. K. Chopra and co-workers at the University of California at Berkeley. The analyses accounted for dam-foundation interaction and water compressibility effects, and considered two loading scenarios: (a) horizontal component of the ground motion and (b) horizontal and vertical components of the ground motion. The results are reported in terms of the maximum expected stresses under extreme loading conditions (maximum credible earthquake, MCE), and they are compared with those results obtained from analyses performed by engineers at the Sacramento District using a response-spectrum-based procedure also developed by Professor Chopra. The influence of the vertical component of the ground motion on the magnitude and distribution of the dynamic stresses is investigated. The levels of tensile demands predicted by this study indicate that localized damage in the form of tensile cracking is likely to take place in limited areas of monoliths 14 and 21 when subjected to extreme seismic loading, but this is still acceptable seismic performance under MCE conditions.

Contents

Conversion Factors, Non-SI to SI Units of Measurement viii

Preface ix

1—Introduction 1

Objective 1
Scope 1
Background 2
Project characteristics 2
Previous analyses 2

2—Selection of Ground Motions 6

Maximum Credible Earthquake 6
Ground Motion Time Histories 6

3—Dynamic Stress Analyses 11

Introduction 11
Material Properties 11
EAGD-84 Analyses 13
Analysis parameters 17
Results – monolith 21 19
Results – monolith 14 33
Comparison with simplified response spectrum analyses 45

4—Conclusions 49

References 51

SF 298

List of Figures

Figure 1. MCE 5-percent-damped horizontal and vertical response spectra 7

Figure 2. 1971 San Fernando earthquake spectrally matched time histories 8

Figure 3. 1979 Imperial Valley earthquake spectrally matched time histories....8

Figure 4. 1986 Chalfant Valley earthquake spectrally matched time histories....9

Figure 5. Comparison of 5-percent-damped horizontal response spectra for truncated time histories....10

Figure 6. Comparison of 5-percent-damped vertical response spectra for truncated time histories....10

Figure 7. Geometry of nonoverflow monolith 21....14

Figure 8. Geometry of overflow monolith 14....14

Figure 9. Finite-element mesh for nonoverflow monolith 21....15

Figure 10. Finite-element mesh for spillway monolith 14 (Model 1)....16

Figure 11. Finite-element mesh for spillway monolith 14 (Model 2)....16

Figure 12. Finite-element mesh for spillway monolith 14 (Model 3)....17

Figure 13. Variation of the wave reflection coefficient as a function of the material parameters of the reservoir bottom material....19

Figure 14. Natural periods and MCE spectra – monolith 21 with rigid foundation....21

Figure 15. Natural periods and MCE spectra – monolith 21 with flexible foundation....21

Figure 16. Static normal stress distribution along dam-foundation interface – monolith 21....22

Figure 17. Static stress S_y – monolith 21 with rigid foundation....23

Figure 18. Static stress S_y – monolith 21 with flexible foundation....23

Figure 19. Maximum principal stress – monolith 21 (heel) – San Fernando earthquake [+H-V]....27

Figure 20. Maximum principal stress – monolith 21 (downstream) – San Fernando earthquake [+H-V]....27

Figure 21. Maximum principal stress – monolith 21 (upstream) – San Fernando earthquake [+H-V]....28

Figure 22. Maximum principal stress – monolith 21 (heel) – Imperial Valley earthquake [-H-V]....28

Figure 23. Maximum principal stress – monolith 21 (downstream) – Imperial Valley earthquake [-H-V]....29

Figure 24. Maximum principal stress – monolith 21 (upstream) – Imperial Valley earthquake [-H-V]....29

Figure 25. Maximum principal stress – monolith 21 (heel) – Chalfant earthquake [+H+V]....30

Figure 26. Maximum principal stress – monolith 21 (downstream) – Chalfant earthquake [+H+V] 30

Figure 27. Maximum principal stress – monolith 21 (upstream) – Chalfant earthquake [+H+V] 31

Figure 28. Normal vertical stress S_y – monolith 21 – San Fernando earthquake [+H-V] 31

Figure 29. Normal vertical stress S_y – monolith 21 – Imperial Valley earthquake [-H-V] 32

Figure 30. Normal vertical stress S_y – monolith 21 – Chalfant earthquake [+H+V] 32

Figure 31. Distribution of maximum total (blue) and dynamic (red) normal vertical stresses along the upstream face of monolith 21 – San Fernando earthquake – cases [+H] and [+H-V] 33

Figure 32. Distribution of maximum total (blue) and dynamic (red) normal vertical stresses along the upstream face of monolith 21 – Imperial Valley earthquake – cases [-H] and [-H-V] 34

Figure 33. Distribution of maximum total (blue) and dynamic (red) normal vertical stresses along the upstream face of monolith 21 – Chalfant earthquake – cases [+H] and [+H+V] 34

Figure 34. Natural periods and MCE spectra – monolith 14 with rigid foundation 36

Figure 35. Natural periods and MCE spectra – monolith 14 with flexible foundation 37

Figure 36. Static normal stress distribution along dam-foundation interface – monolith 14 38

Figure 37. Static stress S_y – monolith 14 with rigid foundation 38

Figure 38. Static stress S_y – monolith 14 with flexible foundation 39

Figure 39. Maximum principal stress – monolith 14 (heel) – San Fernando earthquake [+H-V] 40

Figure 40. Maximum principal stress – monolith 14 (heel) – Imperial Valley earthquake [-H-V] 41

Figure 41. Maximum principal stress – monolith 14 (heel) – Chalfant earthquake [+H+V] 41

Figure 42. Normal vertical stress S_y – monolith 14 – San Fernando earthquake [+H-V] 42

Figure 43. Normal vertical stress S_y – monolith 14 – Imperial Valley earthquake [-H-V] 42

Figure 44. Normal vertical stress S_y – monolith 14 – Chalfant earthquake [+H+V] 43

Figure 45. Distribution of maximum total (blue) and dynamic (red) normal vertical stresses along the upstream face of monolith 14 – San Fernando earthquake – cases [+H] and [+H-V] 44

Figure 46. Distribution of maximum total (blue) and dynamic (red) normal vertical stresses along the upstream face of monolith 14 – Imperial Valley earthquake – cases [-H] and [-H-V] 44

Figure 47. Distribution of maximum total (blue) and dynamic (red) normal vertical stresses along the upstream face of monolith 14 – Chalfant earthquake – cases [+H] and [+H+V] 45

Figure 48. Comparison of maximum values of dynamic normal vertical stresses along the upstream face of monolith 21 obtained by simplified response spectrum analysis (black) and time-history analysis (red) 46

Figure 49. Comparison of maximum values of dynamic normal vertical stresses along the upstream face of monolith 14 obtained by simplified response spectrum analysis (black) and time-history analysis (red) 46

Figure 50. Maximum dynamic normal vertical stresses along the width of the upstream face of monolith 14 obtained by simplified response spectrum analysis (black) and time-history analysis (red) 48

List of Tables

Table 1. Input Ground Motions Used in the Analyses 7

Table 2. Duration Parameters for Horizontal Components of Input Ground Motions 9

Table 3. Material Parameters for Mass Concrete 11

Table 4. Material Parameters for Foundation Rock 12

Table 5. Material Parameters Used in Finite-Element Models 17

Table 6. Natural Frequencies – Monolith 21 with Rigid Foundation (Empty Reservoir) 20

Table 7. Natural Frequencies – Monolith 21 with Flexible Foundation (Empty Reservoir) 20

Table 8. Peak Values of Maximum Principal Stresses – Monolith 21 – San Fernando Earthquake 24

Table 9. Peak Values of Maximum Principal Stresses – Monolith 21 – Imperial Valley Earthquake 24

Table 10. Peak Values of Maximum Principal Stresses – Monolith 21 – Chalfant Earthquake 25

Table 11. Natural Frequencies – Monolith 14 with Rigid Foundation (Empty Reservoir) 35

Table 12. Natural Frequencies – Monolith 14 with Flexible Foundation (Empty Reservoir) 36

Table 13. Peak Values of Maximum Principal Stresses – Monolith 14 – San Fernando Earthquake 39

Table 14. Peak Values of Maximum Principal Stresses – Monolith 14 – Imperial Valley Earthquake 39

Table 15. Peak Values of Maximum Principal Stresses – Monolith 14 – Chalfant Earthquake 40

Conversion Factors, Non-SI to SI Units of Measurement

Non-SI units of measurements used in this report can be converted to SI unit as follows:

Multiply	By	To Obtain
cubic feet	0.028317	cubic meters
Fahrenheit degrees	(F-32)/1.8	Celsius degrees
feet	0.304800	meters
gallons	0.00378	cubic meters
grams	0.001	kilograms
inches	25.4	millimeters
miles	1.609	kilometers
ounces	0.00002957	cubic meters
pounds (force) per square inch	0.006894757	megapascals
pounds (mass) per cubic foot	16.01846	kilograms per cubic meter
square inches	6.4516	square centimeters

Preface

This report describes a research study developed by the U.S. Army Engineer Research and Development Center (ERDC) consisting of dynamic stress analyses performed on monoliths 14 and 21 of Folsom Dam, California. These monoliths were chosen as representative of critical overflow and nonoverflow configurations. The analyses were conducted using the computer program EAGD-84, developed by Professor A. K. Chopra and co-workers at the University of California at Berkeley. The results from these analyses complement the information provided by other previous and current technical studies, and it is expected that they will contribute toward a more accurate assessment of the seismic performance of this critical structure. The study was part of the Civil Works Direct-Allotted 354 Infrastructure Technologies R&D Program, Work Unit 33013, "Rehabilitation of Concrete Hydraulic Structures Under Extreme Loads," which is sponsored by Headquarters, U.S. Army Corps of Engineers.

This publication was prepared by personnel from the ERDC, Geotechnical and Structures Laboratory (GSL), Vicksburg, MS. The research described herein was conducted by Dr. Enrique E. Matheu and Mr. Raju V. Kala, Geotechnical and Earthquake Engineering Branch (GEEB), and Dr. Robert L. Hall, Chief, Geosciences and Structures Division (GSD), GSL. Dr. Matheu prepared this publication under the general supervision of Dr. David W. Pittman, Acting Director, GSL; Dr. Robert L. Hall, Chief, Geosciences and Structures Division, GSL; and Dr. Joseph P. Koester, Chief, GEEB, GSL.

At the time of publication of this report, COL James R. Rowan, EN, was Commander and Executive Director of ERDC, and Dr. James R. Houston was Director.

1 Introduction

Objective

The objective of the technical work documented in this report is to evaluate the dynamic response of Folsom Dam in the event of the Maximum Credible Earthquake (MCE). This technical study included two-dimensional dynamic stress analyses of representative sections of the concrete dam. The U.S. Army Engineer District, Sacramento (SPK), commissioned this study to determine the expected structural performance of the main concrete dam under extreme loading conditions. An important objective is to compare the results obtained in this study by conducting time-history finite-element analyses of two-dimensional sections with the corresponding results calculated by the Sacramento District using response-spectrum-based analyses of three-dimensional models. The results and conclusions presented in this report are intended to complement the information provided by other previous and current technical studies, and it is expected that they will contribute towards a more accurate assessment of the seismic performance of this critical structure.

Scope

This report presents the results of a series of finite-element-based dynamic stress analyses of selected two-dimensional sections of Folsom Dam. The selected sections corresponded to monoliths 14 and 21 of the main concrete dam. Sacramento District's technical personnel selected these two monoliths (14 and 21) as representative of the most relevant dynamic response characteristics of critical overflow and nonoverflow sections of the concrete dam, respectively. The analyses are performed using well-recognized linear time-history response procedures and the results include the maximum expected stresses under extreme loading conditions (MCE), accounting for dam-foundation interaction and water compressibility effects. The results from this numerical study complement previous analyses performed by the Sacramento District using the simplified analysis procedure developed by Professor Anil K. Chopra (Chopra 1978, Fenves and Chopra 1986, Chopra and Hanchen 1989).

Background

Project characteristics

Folsom Dam is located on the American River, about 20 miles northeast of the city of Sacramento, CA. The reservoir is used not only to provide flood control, but it also serves for irrigation and power generation purposes. The maximum height of the gravity dam section is 340 ft[1] with a crest length of about 1,400 ft. It consists of 28 monoliths, 50 ft wide each, and its construction was completed in 1956. The monoliths were constructed in 5-ft lifts and are founded in hard granodiorite rock. A 2- to 10-ft-thick shell of concrete with relatively high cement content (rich concrete) was placed along the upstream and downstream faces of the monoliths from the base to the crest. A concrete mix with lower cement content (lean concrete) was placed throughout the rest of the dam section (Hall et al. 1989).

The motivation of the Folsom Dam Outlet Works Modifications Project is to reduce the risk of flooding to the city of Sacramento posed by the American River. Specifically, the objective of this project is to increase the current outflow capability from 26,000 to 115,000 ft^3/sec at the reservoir water-surface elevation corresponding to the spillway crest. This increased release capacity will lead to a more efficient use of the flood reservation space, and will increase the overall level of downstream flood protection by reducing the probability of flooding in Sacramento in any one year from one chance in 100 to one chance in 140. The project basically consists of enlarging the four existing upper tier river outlets from 5 ft wide by 9 ft high to 9.33 ft wide by 14 ft high, constructing two new upper tier river outlets of the same size, and enlarging the four existing lower tier river outlets from 5 ft wide by 9 ft high to 9.33 ft wide by 12 ft high (Wong et al. 2002).

Previous analyses

The Corps conducted a series of comprehensive seismic evaluation studies of the dam in the late 1980s. These studies included stress and global stability analyses of critical sections of the main concrete dam (Hall et al. 1989). The MCE was defined as an event of magnitude 6.5 at a source-to-site distance of about 15 km, on the eastern branch of the Bear Mountains fault zone. The corresponding peak ground acceleration (PGA) for the horizontal direction was defined as 0.35 g, and two different horizontal ground acceleration time histories were selected for the dynamic analyses. The corresponding vertical ground acceleration time histories were generated by increasing the frequency content by a factor of 1.5 and reducing the amplitudes by a factor of 0.60.

The dynamic stress analyses were performed using the computer program EAGD-84. Preliminary analyses of several cross sections revealed that the tallest nonoverflow monolith represented the critical section. The results from

[1] A table of factors for converting non-SI units of measurement to SI units is presented on page viii.

additional analyses, considering different values of foundation modulus (5.8, 7.9, and $11.0 \cdot 10^6$ psi) and wave reflection coefficient (0.75, 0.79, and 0.82) as well as all possible sign combinations for the ground motion pairs, indicated that the stresses due to the MCE were within a range deemed acceptable. The most demanding condition, characterized by the largest values of the foundation modulus and the wave reflection coefficient, resulted in a maximum principal stress that reached a peak value of 871 psi. This peak value occurred on the downstream face, near the lower end of the circular transition.

This study also included a global stability analysis of the tallest nonoverflow monolith. This analysis was performed using a seismic coefficient of 0.15 to pseudo-statically represent the lateral inertial forces acting on the monolith. The shear strength values used in the analysis were based on typical values and included a significant contribution from cohesion at the dam-foundation interface. The computed factors of safety against sliding were considered acceptable, but some of the underlying assumptions would not be presently considered valid based on current guidelines for analysis.

As part of the Folsom Dam Outlet Works Modification Project, the seismic performance of Folsom Dam was evaluated by global stability and stress analyses of selected monoliths performed by the Sacramento District. The earthquake excitation was defined according to probabilistic and deterministic seismic hazard analyses based on the most current data available (URS Corporation 2001; URS Corporation 2002). Stress analyses of monoliths 13, 14, and 21 consisted of the application of Chopra's simplified response spectrum procedure. This approach was used to determine two sets of earthquake lateral forces associated with the imposed upstream-downstream base motion (the method was later expanded to consistently include the effects of vertical ground motion). The first set of forces corresponds to the lateral inertia forces associated with the fundamental vibration mode of the two-dimensional model of the monolith, considering dam-water interaction, water compressibility, reservoir bottom absorption, and dam-foundation rock interaction effects. The second set of forces corresponds to the lateral earthquake forces associated with higher vibration modes of the system. An underlying assumption in the simplified procedure used to determine the earthquake forces is that the monolith is supported on a horizontal surface of underlying flexible foundation rock. This is certainly appropriate for monoliths 14 and 21, which exhibit a dam/foundation contact with approximately uniform elevations. However, in the case of monolith 13, the dam/foundation contact varies by as much as 35 ft in elevation, and it was necessary to assume a horizontal base based on the average monolith height.

The earthquake-induced lateral forces were applied to three-dimensional (3D) finite element models of the spillway monoliths, developed using the computer program GT STRUDL. Taking advantage of symmetry conditions, detailed 3D models were developed for only half (25 ft) of the corresponding width, and they included the corresponding conduits and chamber openings. In the analysis of the spillway monoliths, two different models were generated to adequately reflect existing and modified (enlarged chambers and conduits) conditions. To facilitate the meshing, some minor simplifications were incorporated in the geometry of the conduits and the spillway pier. In particular,

the spillway pier was modeled assuming a reduced thickness of 5 ft (existing condition) and 6 ft (modified condition), instead of the actual thickness of 8 ft. Both the mass density and the elastic modulus of the pier concrete were adjusted by a factor equal to the ratio between the actual and assumed widths. This approach appropriately captures the influence of the pier in the global dynamic characteristics of the section, and it is justified in those cases where the goal of the analysis is the determination of the stresses within the mass concrete. For all cases analyzed, dry downstream conditions were assumed (no tailwater) and the reservoir pool elevation was assumed at gross pool elevation (466.0 ft).

Based on the eigenvalue analyses of the 3D finite-element models, the computed fundamental vibration period of monolith 14 (modified condition) on rigid foundation rock with empty reservoir was 0.163 sec. After taking into account the effects of water and foundation-rock flexibility according to the simplified procedure, the resulting value of the fundamental vibration period was 0.308 sec. For monolith 21, the computed fundamental vibration period was 0.183 sec, corresponding to rigid foundation rock and empty reservoir conditions. This value increased to 0.261 sec after incorporating water and foundation-rock flexibility effects according to the simplified procedure.

Estimates of the peak seismic responses were obtained by performing static analysis of the 3D models subjected to the two sets of earthquake-induced lateral forces and combining the corresponding responses using the square-root-of-the-sum-of-squares (SRSS) rule. These peak values were then combined with the static effects (dead weight, hydrostatic pressure, and uplift) to provide total response estimates. The results indicated a few localized areas with important tensile demands. For example, the results for monolith 14 (modified condition) showed peak vertical tensile stresses within the apparent dynamic tensile strength of the mass concrete (700 psi), except for a stress concentration of 1,143 psi at the upstream heel of the monolith (corresponding to the case of static loads plus horizontal and vertical components of the ground motion). This stress drops sharply to values below the tensile strength within a distance of 10 ft up above the base. The results for monolith 21 also indicated peak tensile stresses within the apparent dynamic tensile strength of the mass concrete, excepting some areas of stress concentration. For example, the peak vertical stress at the upstream heel reached 893 psi (corresponding to the case of static loads plus horizontal and vertical components of the ground motion), but the value quickly drops below the tensile strength within a distance of 10 ft up from the base. In spite of the fact that these stress concentrations may be accentuated by the assumed fixed boundary condition at the dam base, high tensile stresses are very likely to occur at these localized regions. However, even if cracking occurs in these areas, the extent of damage is expected to be limited and this is still considered as acceptable MCE performance.

Global stability analyses were performed for monoliths 12 through 20. The studies included two-dimensional (2D) conventional stability analyses (determination of factor of safety against sliding and percentage of base in compression), conducted in compliance with EM 1110-2-2200 (Headquarters, U.S. Army Corps of Engineers (HQUSACE) 1995), and computation of permanent displacement estimates, following the procedure indicated in

EM 1110-2-6050 (HQUSACE 1999). Two possible failure surfaces were considered: a concrete lift joint near the base of the dam (lift joint failure), and a horizontal plane in the rock mass at (or just below) the dam-foundation contact (near contact failure). The possibility of a more complex failure mode occurring within the rock mass is currently under investigation. For the seismic load cases, the reservoir pool elevation was assumed at 446 ft. This value was based on historical data and it represents the average for the high three months (May, June, July). Tailwater level was assumed at elevation 160 ft. Uplift pressures were computed assuming a drain efficiency of 50 percent for all monoliths investigated, excepting monolith 15, for which 60-percent drain efficiency was assumed based on actual piezometer data. Each monolith was analyzed considering two sets of shear strength parameters, depending on the assumed failure surface. For lift joint failure, a cohesion value of 300 psi and a friction angle of 50 deg were selected for all monoliths. For near contact failure, zero cohesion was considered and the friction angle was computed as a combination of a basic rock-on-rock friction angle (30 deg) and a dilatancy angle representing localized conditions below each monolith. Based on this approach, a friction angle of 55 deg was determined for the analysis of near contact failure in all monoliths, with the exception of monoliths 15 and 16, which were assigned friction angles of 44 deg and 53 deg, respectively. For seismic load cases, acceptable values of factors of safety were found for almost all the monoliths investigated, with the exception of monolith 15. The computed sliding factor of safety under MCE conditions was 1.0, and therefore this monolith did not meet the corresponding MCE sliding stability criteria. However, based on the computed estimates of sliding permanent displacement (less than 1 in.), its performance was considered acceptable.

2 Selection of Ground Motions

Maximum Credible Earthquake

The earthquake excitation was specified by the Sacramento District according to the most recent seismic hazard studies. These studies defined the controlling MCE as an event of magnitude 6.5 at a source-to-site distance of 14 km, on the eastern branch of the Bear Mountains fault zone. Based on this, the characterization of the corresponding site ground motions was performed by considering four different attenuation relationships. The peak horizontal ground acceleration values corresponding to the median (50^{th} percentile) and median plus one standard deviation (84^{th} percentile) were determined as 0.24 g and 0.38 g, respectively (URS Corporation 2001). Based on the magnitude and distance of the MCE, it was concluded that faults directivity effects were not significant and the same response spectrum was specified for the two horizontal components.

The corresponding vertical response spectrum was initially defined by uniform scaling of the MCE horizontal spectrum using a reduction factor of 2/3 (URS Corporation 2002). Therefore, the vertical response spectrum was determined based on a constant factor for all periods. This recommendation was later modified and the resulting vertical response spectrum was defined using a period-dependent scaling factor (URS Corporation 2003). The resulting 5-percent-damping response spectra for horizontal and vertical motion are shown in Figure 1.

Ground Motion Time Histories

Three sets of earthquake time histories, each consisting of three components, were developed for the MCE (URS Corporation 2002, 2003). These time histories were generated by modifying a suite of recorded ground motions so their response spectra would match the corresponding 5-percent-damping response spectra shown in Figure 1. The earthquake records used to develop the spectrally matched time histories are presented in Table 1. Out of the two horizontal components for each time history, the one associated with the largest peak ground velocity (PGV)

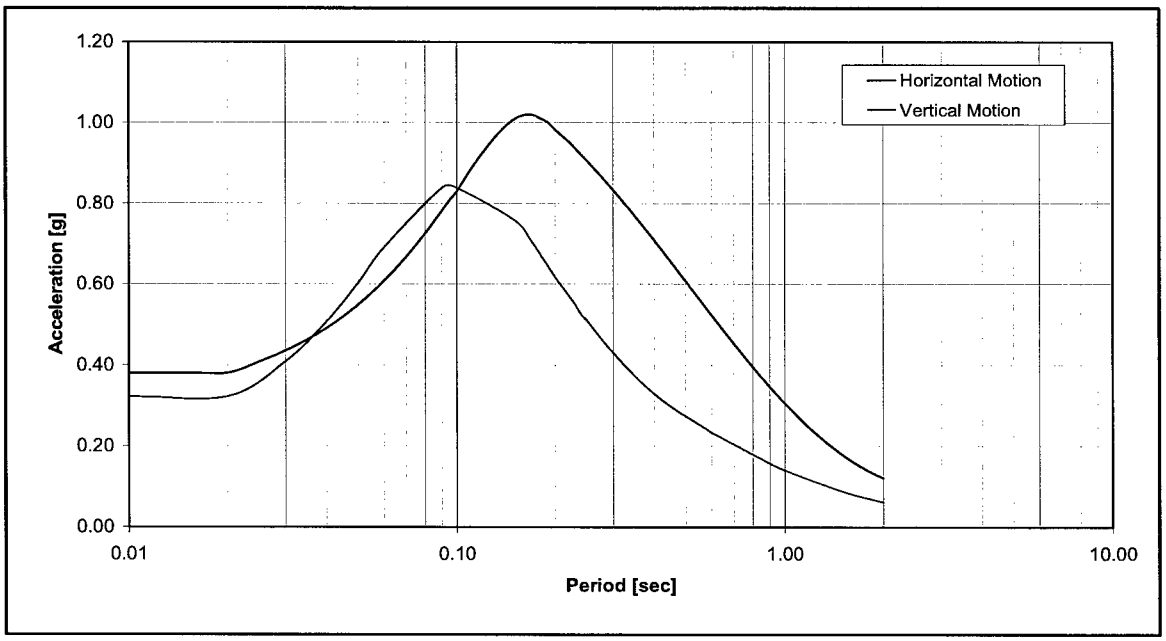

Figure 1. MCE 5-percent-damped horizontal and vertical response spectra

Table 1
Input Ground Motions Used in the Analyses

Earthquake	Recorded Ground Motions					Modified Time Histories		
	Mw	Station	Dist. (km)	Comp.	PGA (g)	PGA (g)	PGV (cm/sec)	Direction
1971 San Fernando	6.6	Pasadena – Old Seism. Lab.	19	180	0.09	0.38	27.0	Cross Ch.
				270	0.20	0.38	34.8	Us/Ds
				Vertical	0.09	0.30	13.5	Vertical
1979 Imperial Valley	6.5	Cerro Prieto	26	147	0.17	0.38	23.8	Us/Ds
				237	0.16	0.38	23.1	Cross Ch.
				Vertical	0.21	0.33	11.5	Vertical
1986 Chalfant Valley	6.2	Bishop – Paradise Lodge	23	70	0.16	0.38	28.8	Cross Ch.
				160	0.16	0.38	29.4	Us/Ds
				Vertical	0.13	0.31	11.7	Vertical

was selected as the horizontal upstream-downstream component to be used in the two-dimensional analyses. Figures 2 through 4 show the selected horizontal and vertical components for the spectrally matched time histories.

The initial phase in the evaluation of the seismic performance of a concrete gravity section using linear time-history analysis is primarily concerned with the determination of the peak values of relevant response quantities, such as the maximum principal tensile stresses, and their spatial distribution. For the purpose of determination of peak responses, the same duration of analysis (30 sec) was used for the three sets of input motions considered in this study. The decision to use a uniform duration for all cases was made based on preliminary analyses that showed that this duration was adequate to bracket the peak values and capture the

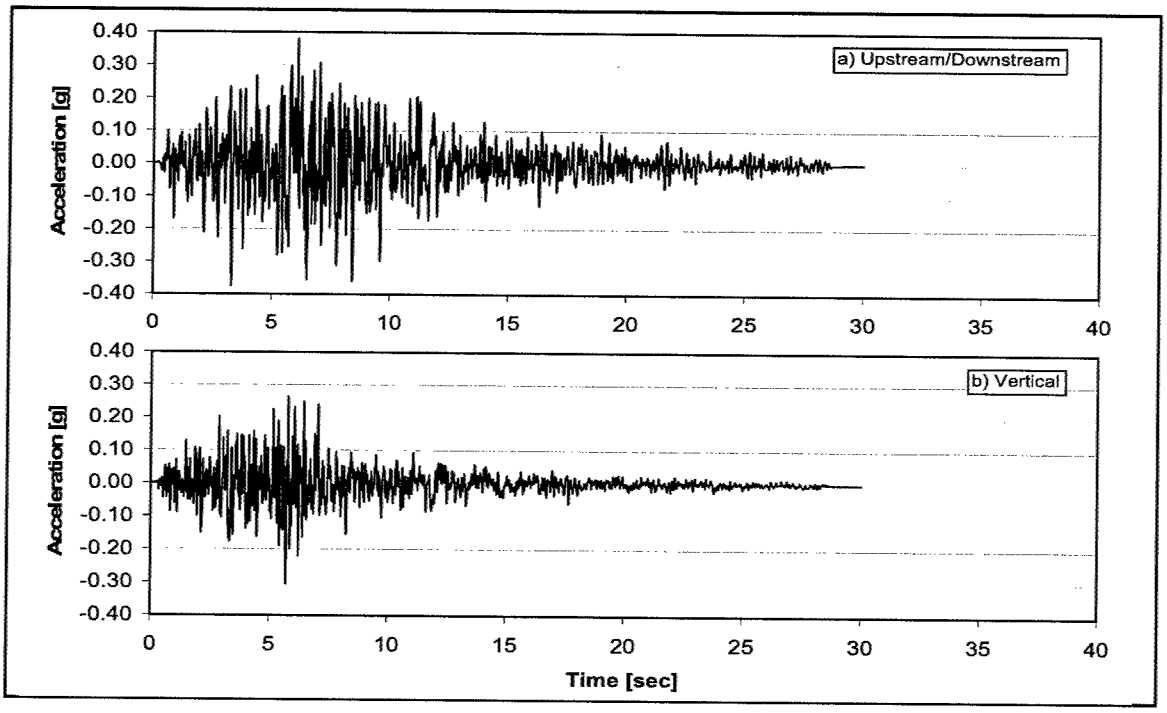

Figure 2. 1971 San Fernando earthquake spectrally matched time histories

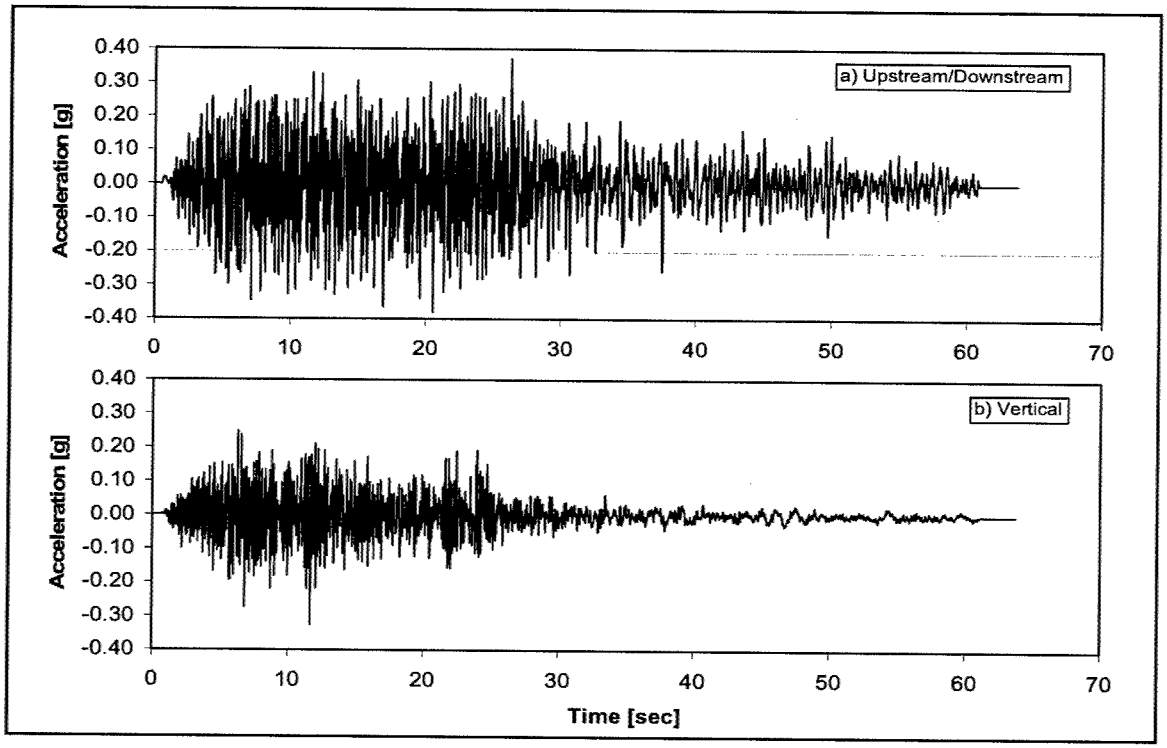

Figure 3. 1979 Imperial Valley earthquake spectrally matched time histories

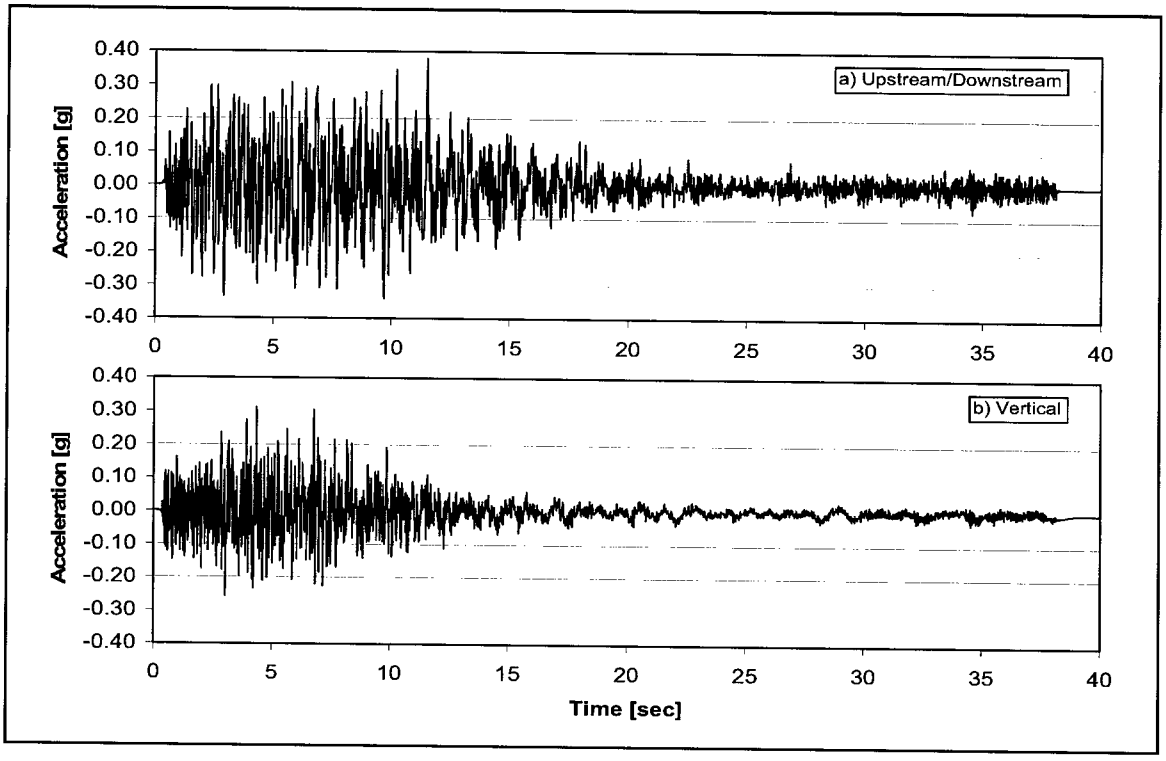

Figure 4. 1986 Chalfant Valley earthquake spectrally matched time histories

relevant features of the response. Table 2 shows a comparison of the duration parameters corresponding to the horizontal components of the selected input ground motions for the original records and for the 30-sec truncated records. Figures 5 and 6 highlight the close match between the individual response spectra for the 30-sec truncated input time histories and the corresponding targets for the horizontal and vertical directions, respectively.

Table 2
Duration Parameters for Horizontal Components of Input Ground Motions

Parameter	Original records			Truncated records (30 [sec])		
	San Fernando	Imperial Valley	Chalfant	San Fernando	Imperial Valley	Chalfant
Total Arias Intensity I_a, in/sec	103.15	321.02	140.17	103.15	265.33	138.16
Starting Time (5 percent I_a), sec	2.24	4.88	1.74	2.24	4.54	1.71
Ending Time (95 percent I_a), sec	16.30	44.36	17.35	16.30	27.40	16.08
Arias Intensity Duration $T_{Ia(5\text{-}95)}$, sec	14.06	39.48	15.61	14.06	22.86	14.36
Bracketed Duration $T_{0.05}$, sec	22.35	57.37	35.12	22.35	28.53	29.53

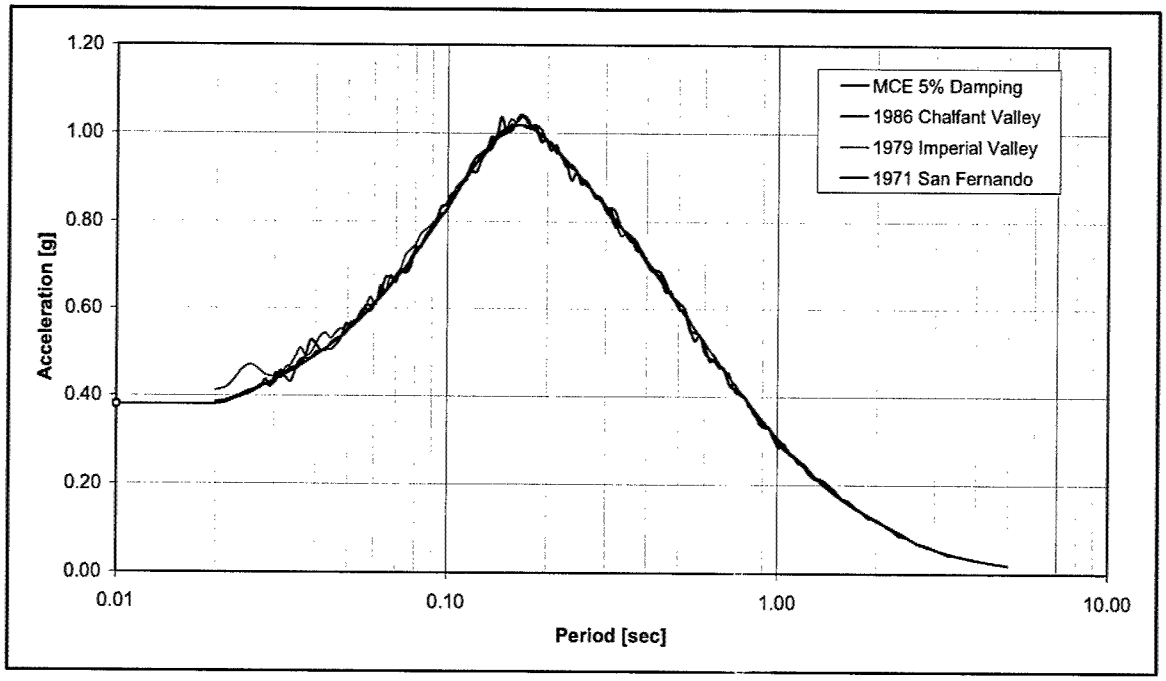

Figure 5. Comparison of 5-percent-damped horizontal response spectra for truncated time histories

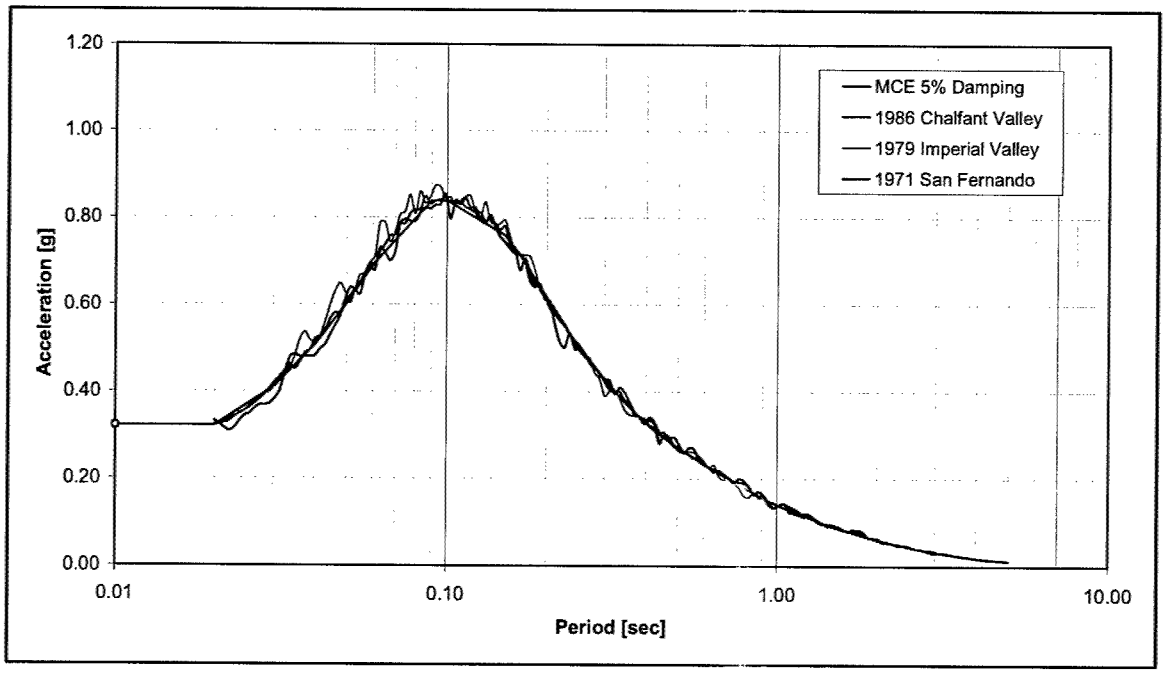

Figure 6. Comparison of 5-percent-damped vertical response spectra for truncated time histories

3 Dynamic Stress Analyses

Introduction

This section presents the results of the dynamic stress analyses performed on two-dimensional (2D) finite-element models of monoliths 14 and 21, subject to ground motion time histories that are representative of the MCE. Different analyses are performed using the computer program EAGD-84. The objective of these analyses is not only to quantify the seismic performance of the monoliths by determining the stress responses, but also to investigate the sensitivity of the dynamic response characteristics and corresponding results with respect to variations in the modeling assumptions.

Material Properties

A number of field and laboratory investigations have been performed over the years to characterize the material parameters of the mass concrete and the foundation rock. Table 3 summarizes some of the relevant material properties for the mass concrete, as defined by the Sacramento District. Because it is difficult to accurately define the thickness of the layer of rich concrete, it is assumed that the mass concrete is characterized by the material properties corresponding to the lean concrete mix.

Table 3
Material Parameters for Mass Concrete

Material Property	Value
Unit weight γ_c, pcf	158
Concrete compressive strength f_c'	4,375
Splitting tensile strength f_t, psi	360
Static modulus of rupture f_r^{st}, psi	540
Dynamic modulus of rupture f_r, psi	810
Static modulus of elasticity E_c^{st}, psi	$3.6 \cdot 10^6$
Dynamic modulus of elasticity E_c, psi	$5.9 \cdot 10^6$
Poisson's ratio ν_c	0.19

The values indicated above for the unit weight, modulus of elasticity, and Poisson's ratio are the same as those used in a previous seismic evaluation study (Hall et al. 1989) as well as in the stress analyses conducted by the Sacramento District using Chopra's simplified procedure.

The tensile behavior of the mass concrete plays a critical role in the evaluation of the seismic performance of a gravity section, and it is therefore important to understand the basis for the strength value indicated in Table 3. The 1989 study adopted a value of 700 psi for the apparent tensile strength of the lean concrete (this parameter is conceptually equivalent to the dynamic modulus of rupture). This was based on the analysis of a series of static and dynamic split cylinder tests conducted by the U.S. Bureau of Reclamation in 1983 and the University of California at Berkeley in 1986. In 2001, the U.S. Bureau of Reclamation performed a new series of split cylinder tests on 12-in.-diam concrete specimens. The corresponding results indicated an average splitting tensile strength (f_t) of 360 psi for lean concrete (with test values that ranged from 216 to 428 psi). The value of the static modulus of rupture was computed as $f_r^{st} = 1.5 f_t$, and a dynamic increase of 50 percent was assumed for the dynamic modulus of rupture, that is $f_r = 1.5 f_r^{st} = 2.25 f_t$. This leads to the value of 810 psi indicated in Table 2. However, a lower value of tensile strength (700 psi) was considered as the maximum allowable tensile stress for evaluation of the dam performance in the stress analyses conducted by the Sacramento District.

Table 4 summarizes the relevant material properties for the foundation rock, as defined by the Sacramento District. These values correspond to the average values indicated in the 1989 study (Hall et al. 1989), and they were based on the results of a series of geophysical surveys conducted by the Corps of Engineers in 1989. These investigations focused mainly on the left and right abutments of the dam, and it was recognized that, in some cases, the geophysical studies did not penetrate deep enough to substantially engage the foundation rock in all locations tested. In particular, the values of dynamic modulus of elasticity ranged from $5.8 \cdot 10^6$ psi to $11.0 \cdot 10^6$ psi, and the value of $7.9 \cdot 10^6$ psi has been accepted by the Sacramento District as a reasonable estimate for the dynamic modulus of elasticity of the foundation rock at Folsom Dam.

Table 4
Material Parameters for Foundation Rock

Material Property	Value
Unit weight γ_f, pcf	171
Dynamic modulus of elasticity E_f, psi	$7.9 \cdot 10^6$
Poisson's ratio ν_f	0.25

EAGD-84 Analyses

Finite-element models

The EAGD-84 computer program was developed at the University of California at Berkeley to evaluate the seismic response of two-dimensional sections of concrete gravity dams, including the effects of dam-water interaction, dam-foundation rock interaction, and energy absorption effects at the bottom of the reservoir (Fenves and Chopra 1984).

The general analytical model is based on the substructure method, and it assumes linear behavior for the dam-water-foundation system. The resulting equations of motion are solved in the frequency domain. The model assumes a concrete section with a horizontal dam-foundation interface, and constant hysteretic damping is used to represent energy dissipation in the mass concrete. The foundation rock underlying the dam is idealized as a homogeneous, isotropic, visco-elastic half-plane. The water impounded in the reservoir is modeled as a fluid domain of constant depth and infinite length along the upstream direction, and the energy absorption associated with reservoir bottom materials is quantified by a wave reflection coefficient. The earthquake excitation is defined by two components (upstream/downstream and vertical) of the free-field ground acceleration, and the corresponding ground acceleration time-histories are applied at the base of the dam.

Geometry and relevant dimensions of monoliths 21 (nonoverflow) and 14 (overflow) are presented in Figures 7 and 8. The middle cross sections of these monoliths were idealized by two-dimensional finite-element models consisting of four-node quadrilateral elements. The same basic set of material properties was uniformly assigned to the mass concrete, and therefore monolith 21 was modeled with only one material assigned to the whole section. The cross section of this monolith was discretized with 1712 quadrilateral elements, as shown in Figure 9. It is important to notice that the mesh exhibits only eight elements along the dam-foundation interface. As a result of existing limitations in the implementation of the EAGD-84 model, this transition to a reduced number of elements along the dam-foundation contact is necessary to guarantee that the foundation rock is represented by a dynamic stiffness matrix that is fully consistent with the assumption of a visco-elastic half plane. The reduced number of elements at the base of the model will require a careful interpretation of the corresponding stress results. In spite of the fact that this number of elements should be sufficient to capture the general characteristics of the stress distribution at the base of the structure, this modeling limitation will produce underestimation of the stresses in those areas with high stress gradients (such as the heels). Therefore, it will be important to evaluate the stress results not only in terms of their peak values but also in terms of their distribution. This must be also considered when conducting the comparison of these results with those obtained by the Sacramento District using refined 3D models of the monoliths.

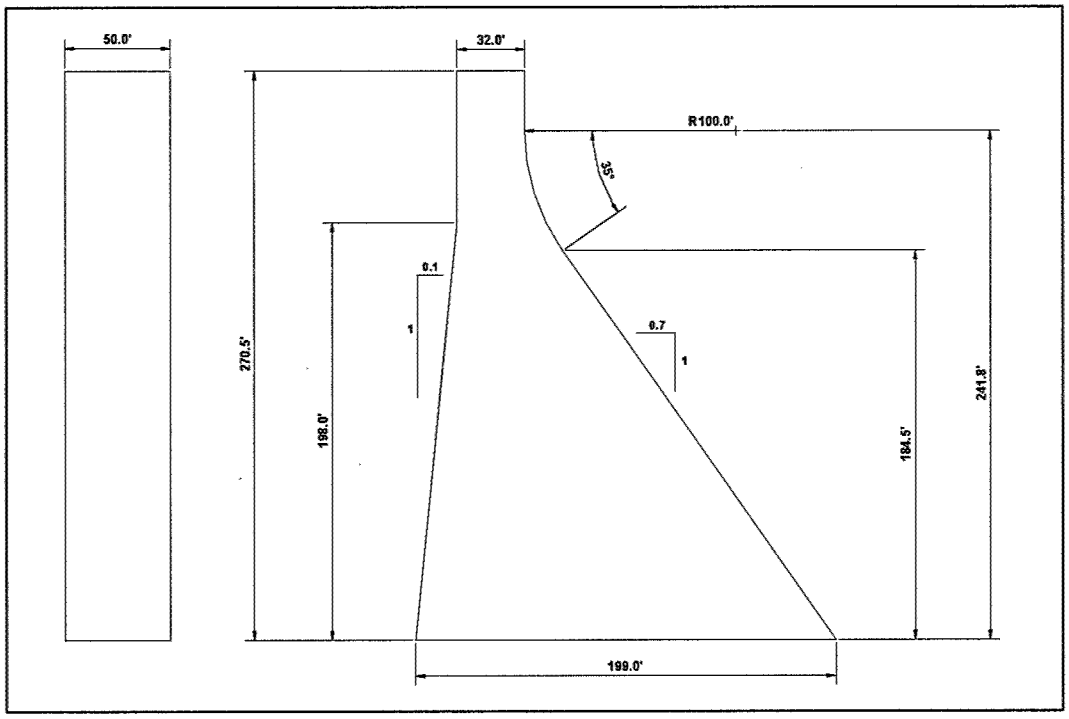

Figure 7. Geometry of nonoverflow monolith 21

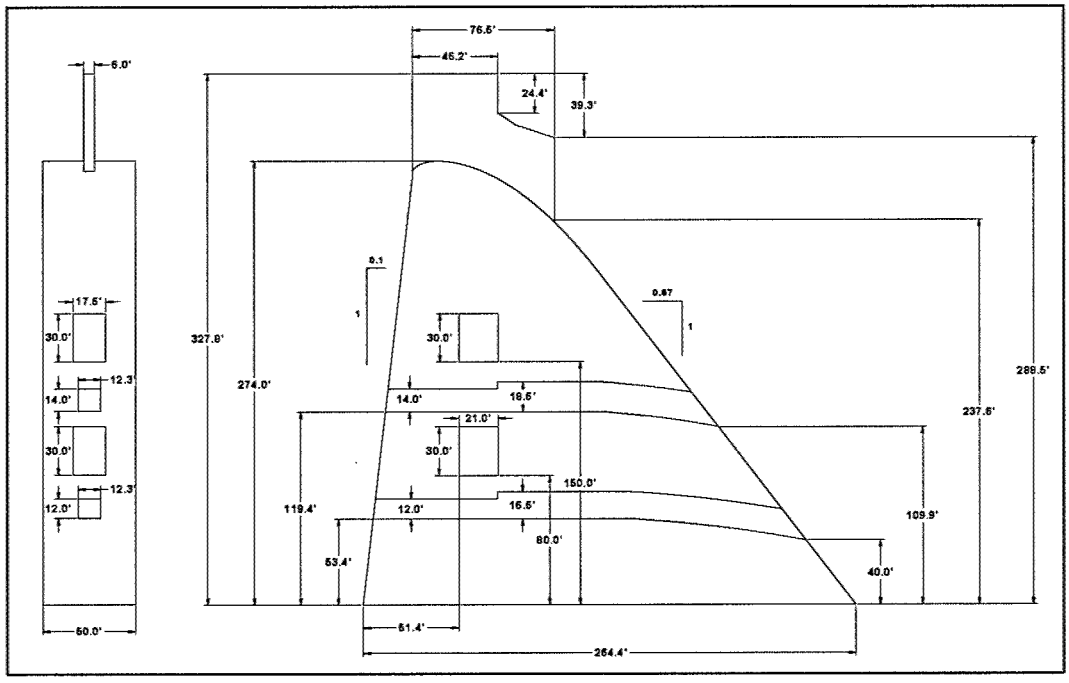

Figure 8. Geometry of overflow monolith 14

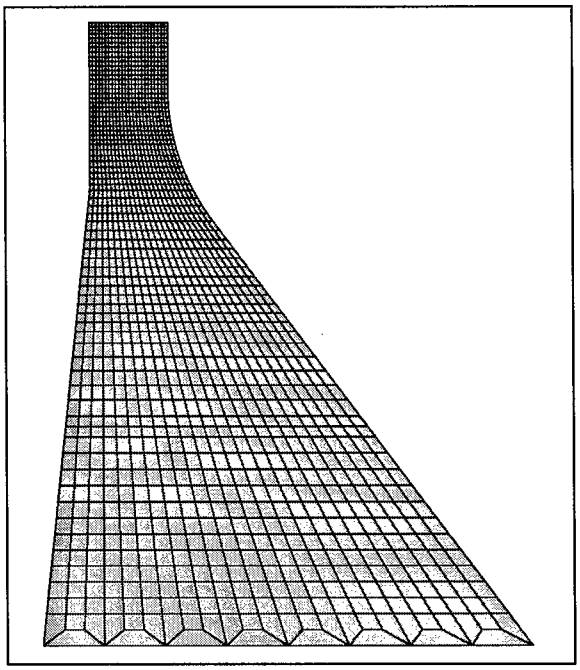

Figure 9. Finite-element mesh for nonoverflow monolith 21

The middle cross section of monolith 14 was discretized with 1936 quadrilateral elements, as shown in Figures 10 through 12. As in the previous case, it becomes necessary to incorporate a transition to a reduced number of elements along the base. In addition, since this is an overflow section, the presence of the spillway pier and the openings corresponding to the upper and lower chambers and conduits must be accounted for in the model. The two-dimensional finite-element models used for these studies are based on the assumption that the section is regular along the direction normal to its plane, i.e., no changes in material properties or dimensions. Therefore, in this case it is necessary to account for the local variations in thickness of the section by appropriately modifying the corresponding material properties. The motivation for this approach is to represent–globally–the effects that these irregularities have on the dynamic characteristics of the section, and it is achieved by introducing equivalent mass and stiffness distributions. Of course, a comprehensive investigation of the stress concentration effects that are induced by the presence of these thickness irregularities would require three-dimensional models such as those used by the Sacramento District in previous studies. Three different finite-element models were developed for monolith 14: (a) the first one accounting only for the presence of the spillway pier (thus ignoring the voids created by the chambers and conduits), (b) the second one considering not only the spillway pier but also the chambers and conduits by means of equivalent material properties, and (c) the third model incorporates the voids corresponding to the chambers while still using equivalent material properties for the pier and the conduits. Table 5 summarizes the material properties used in the finite-element models for monoliths 14 and 21.

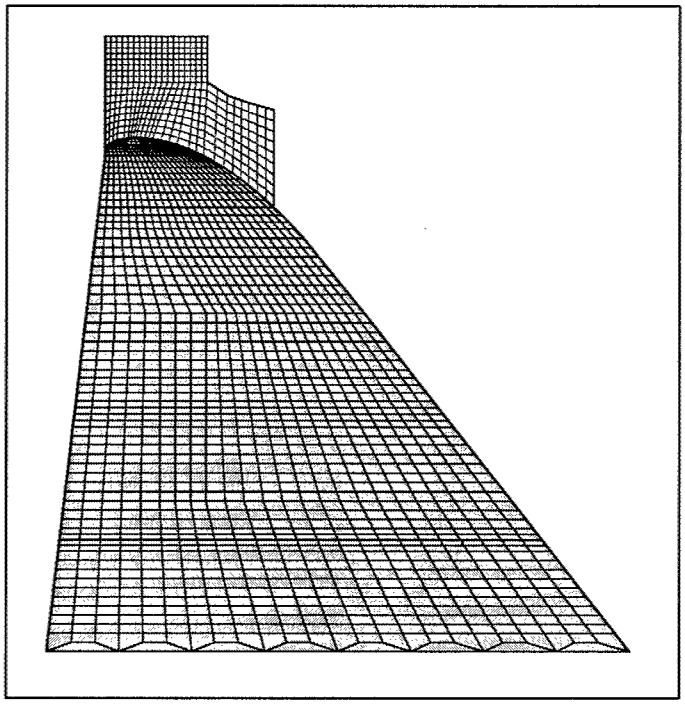

Figure 10. Finite-element mesh for spillway monolith 14 (Model 1)

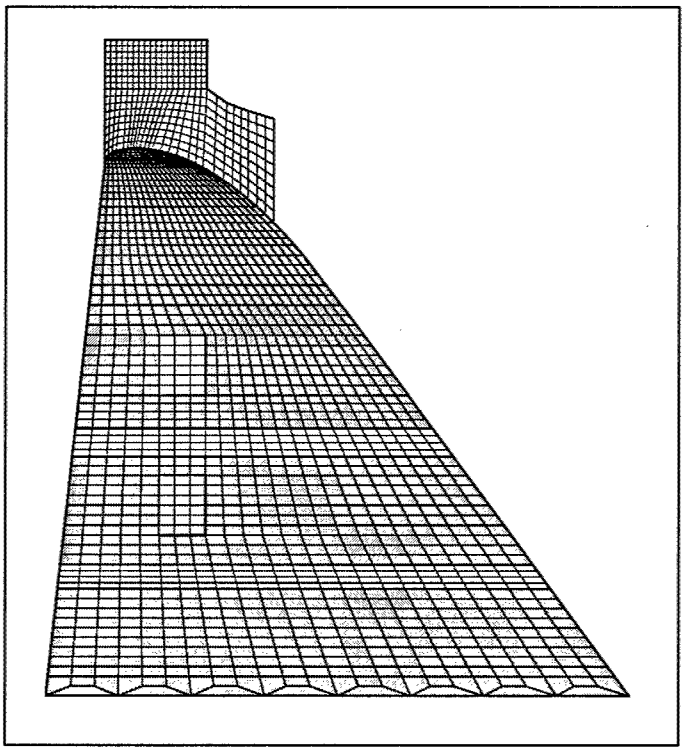

Figure 11. Finite-element mesh for spillway monolith 14 (Model 2)

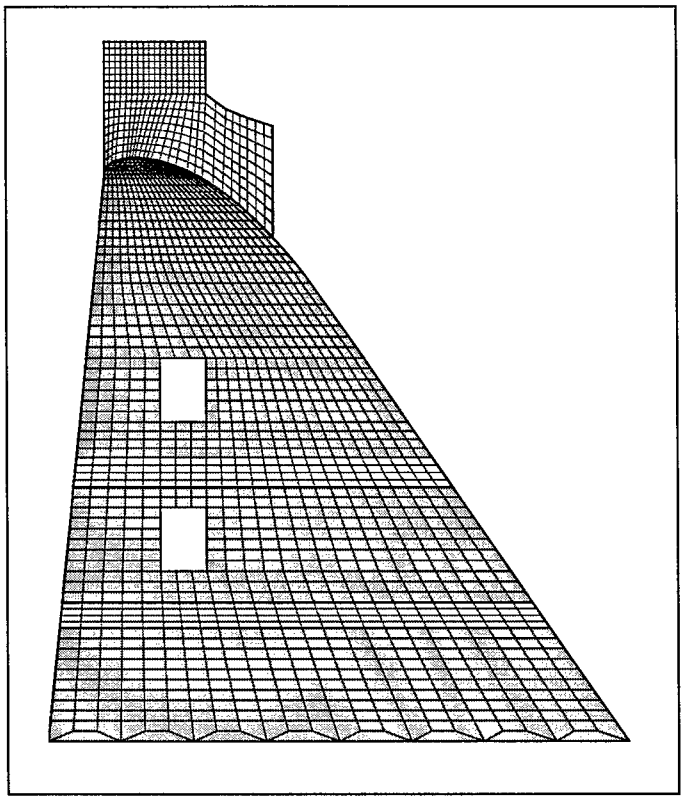

Figure 12. Finite-element mesh for spillway monolith 14 (Model 3)

Table 5
Material Parameters Used in Finite-Element Models

Material Property	Monoliths 14 and 21 (Mass Concrete)	Monolith 14		
		Zone A (Pier)	Zone B (Chambers)	Zone C (Conduits)
Unit weight γ_f, pcf	158	25.3	102.7	119.1
Dynamic modulus of elasticity E_f, psi	$5.9 \cdot 10^6$	$0.94 \cdot 10^6$	$3.84 \cdot 10^6$	$4.45 \cdot 10^6$
Poisson's ratio ν_f	0.19	0.19	0.19	0.19

The dynamic stress analyses described in the next sections included the effects of static loads (self weight and external hydrostatic loads), and the reservoir water surface was assumed at gross pool elevation (466 ft). However, effects of uplift pressures or tailwater were not included in the stress computations presented in this report.

Analysis parameters

In addition to the standard set of material properties described in the previous section, the formulation implemented in the EAGD-84 computer program requires the definition of a series of additional parameters that are not typically

required when using multi-purpose analysis programs such as SAP2000. The most relevant of these parameters is the wave reflection coefficient (α). This coefficient represents the dissipation of hydrodynamic pressure waves in the reservoir bottom. When pressure waves strike the bottom surface, part of the propagating energy is reflected back into the reservoir and another part is transmitted to the foundation medium because of its finite stiffness. This energy may be assumed to continue propagating towards infinity, actually constituting an equivalent energy-dissipating mechanism introducing radiation damping and effectively reducing the system's response. The wave reflection coefficient is defined as follows:

$$\alpha = \frac{1-qC}{1+qC} \tag{1}$$

where C is velocity of pressure waves in water, and q is given by

$$q = \frac{\rho_w}{\rho_r \sqrt{\frac{E_r}{\rho_r}}} \tag{2}$$

In this equation, ρ_w is the mass density of water, that is, $\rho_w = \gamma_w / g$ where γ_w indicates the unit weight and g is the acceleration of gravity. The parameters ρ_r and E_r denote the mass density and elastic modulus of the reservoir bottom material, respectively. Assuming values of 4,730 ft/sec and 62.4 lb/ft^3 for the velocity of pressure waves and unit weight of the water, and assuming that the properties of the reservoir bottom material are the same as those adopted for the foundation rock ($E_r = E_f, \gamma_r = \gamma_f$) as listed in Table 3, a value of 0.79 is obtained for the wave reflection coefficient. This value is representative of energy absorption in the rock material itself, and it does not actually account for any additional absorption due to actual sediment materials deposited at the bottom of the reservoir. It is important to highlight that results from field measurements conducted in 1995 indicated the presence of sediment layers with a significant thickness.

A value of 0.75 was adopted for the wave reflection coefficient in previous seismic evaluation studies conducted by the Sacramento District. This value is also adopted for the stress analyses presented in this report. Figure 13 shows the variation of the wave reflection coefficient as a function of the elastic modulus of the reservoir bottom material, E_r, which is represented in terms of the dimensionless ratio E_r / E_f. The wave reflection coefficient is presented for different values of the mass density of the reservoir bottom materials, which are expressed in terms of the unit weight ratio γ_r / γ_f. Based on the figure, it can be concluded that the value adopted for the previous seismic evaluation studies reasonably represents a range of possible combinations of actual values of E_r and ρ_r at the site.

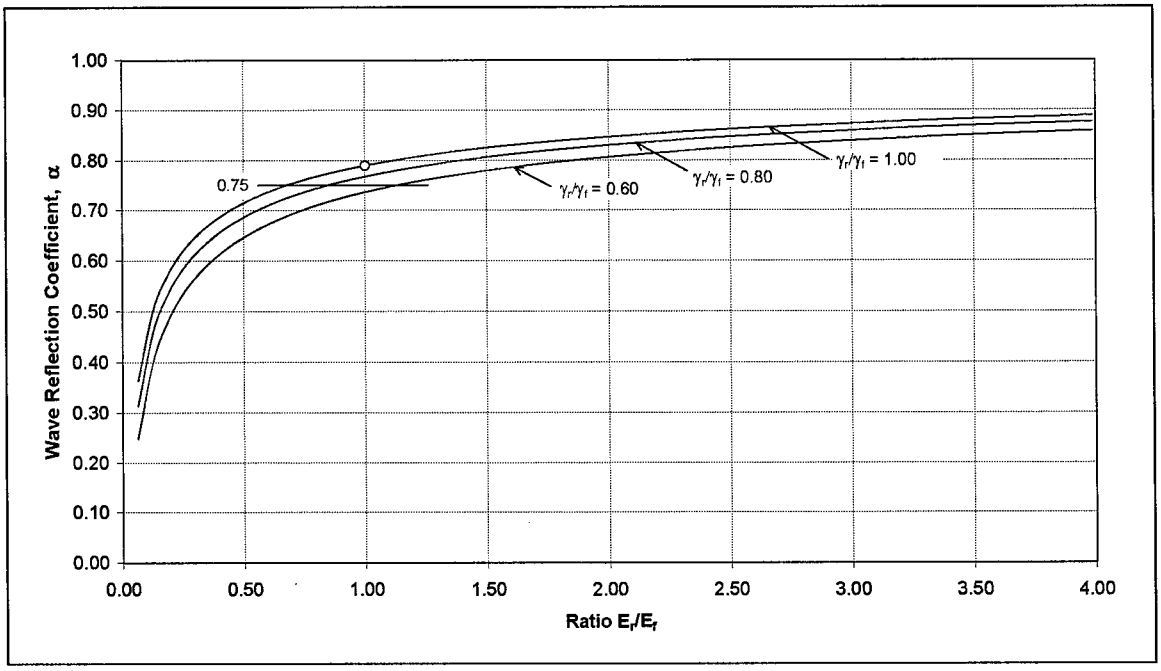

Figure 13. Variation of the wave reflection coefficient as a function of the material parameters of the reservoir bottom material

In addition to the wave reflection coefficient, it is required to quantify two other parameters representing different sources of damping considered in the analysis. One is a constant hysteretic damping model for the dam concrete (η_c) and the other is a constant hysteretic damping model for the foundation rock medium (η_f). A value of hysteretic damping coefficient of 10 percent ($\eta_c = 0.10$) is typically recommended for the dam, and this value corresponds to a 5 percent viscous damping ratio in all vibration modes of the dam. This value is considered suitable for the large motions and associated high stresses expected during strong earthquake shaking. A similar level of hysteretic damping is considered for the foundation rock ($\eta_f = 0.10$), following the same assumptions employed for the previous studies.

Results – monolith 21

Tables 6 and 7 show the first ten natural frequencies for monolith 21, corresponding to empty reservoir conditions and two different foundation conditions. The natural frequencies were calculated for rigid ($E_f = \infty$) and flexible ($E_f = 7.9 \bullet 10^6$ psi) foundation cases. The incorporation of foundation flexibility causes an increase of about 18 percent in the fundamental period of the dam-foundation system with respect to the dam on rigid base. The influence of the flexibility increases all the natural periods, with a significant effect on the period corresponding to the third vibration mode. This mode is associated with a predominantly vertical response of the monolith.

Table 6
Natural Frequencies – Monolith 21 with Rigid Foundation (Empty Reservoir)

Mode	Rigid Foundation	
	Frequency	Period
	[Hz]	[sec]
1	5.44	0.184
2	12.09	0.083
3	16.93	0.059
4	22.53	0.044
5	34.20	0.029
6	36.30	0.028
7	47.54	0.021
8	50.11	0.020
9	52.33	0.019
10	57.77	0.017

Table 7
Natural Frequencies – Monolith 21 with Flexible Foundation (Empty Reservoir)

Mode	Flexible Foundation	
	Frequency	Period
	[Hz]	[sec]
1	4.62	0.217
2	9.12	0.110
3	9.19	0.109
4	16.52	0.061
5	26.66	0.038
6	27.59	0.036
7	39.83	0.025
8	42.74	0.023
9	45.01	0.022
10	51.24	0.020

Figures 14 and 15 show the location of the first five natural periods with respect to the MCE 5-percent-damped horizontal and vertical response spectra. Figure 13 corresponds to rigid foundation conditions, whereas Figure 14 represents the effects of foundation flexibility. It is important to mention that these natural periods correspond to empty reservoir conditions (as computed by EAGD-84), and that the actual dynamic response characteristics of the system will be affected by the corresponding hydrodynamic effects.

Figure 16 shows the distribution of static normal vertical stress (S_y) along the dam-foundation interface, considering only self-weight and hydrostatic loading. The results are presented for both rigid and flexible foundation conditions. The standard stress output in EAGD-84 corresponds to the element centers, and these values were averaged between adjacent elements along the dam-foundation interface to compute the corresponding nodal values. The stress values for the heel and toe nodes were computed by linear extrapolation. The figure shows that for the assumed reservoir level (gross pool elevation at 466 ft), the static normal stress at the heel of the dam reaches values of 60 and -65 psi, for rigid and flexible base conditions, respectively. The distribution of the normal stress S_y across the section

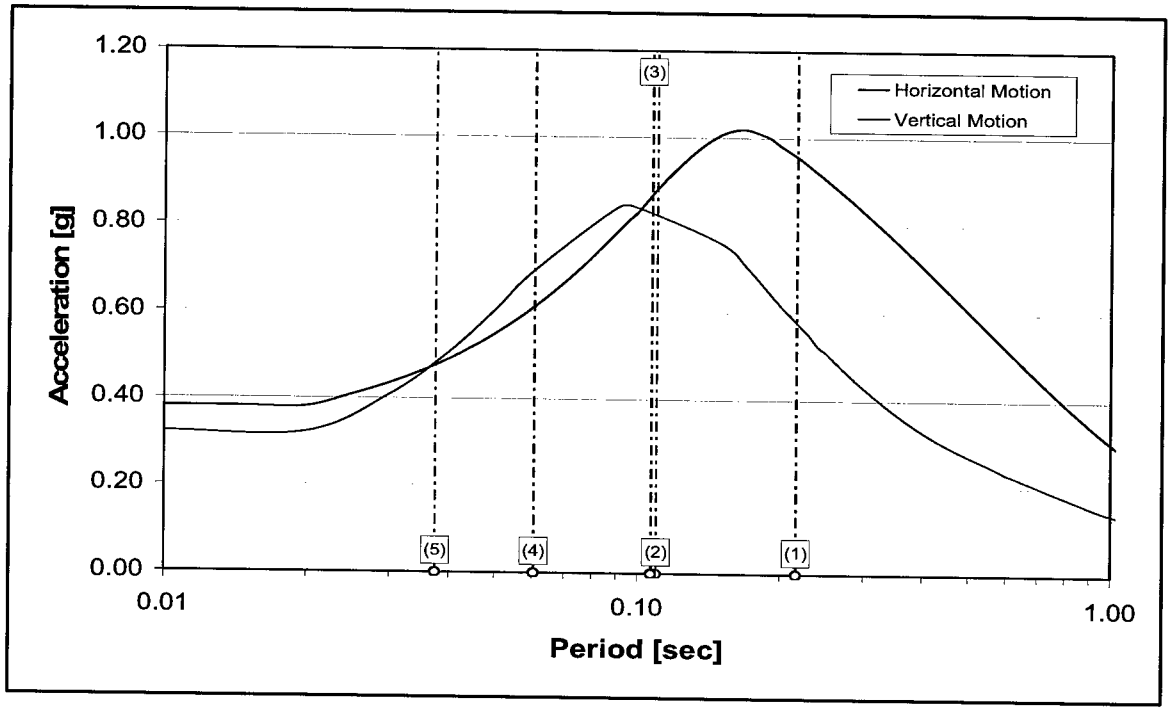

Figure 14. Natural periods and MCE spectra – monolith 21 with rigid foundation

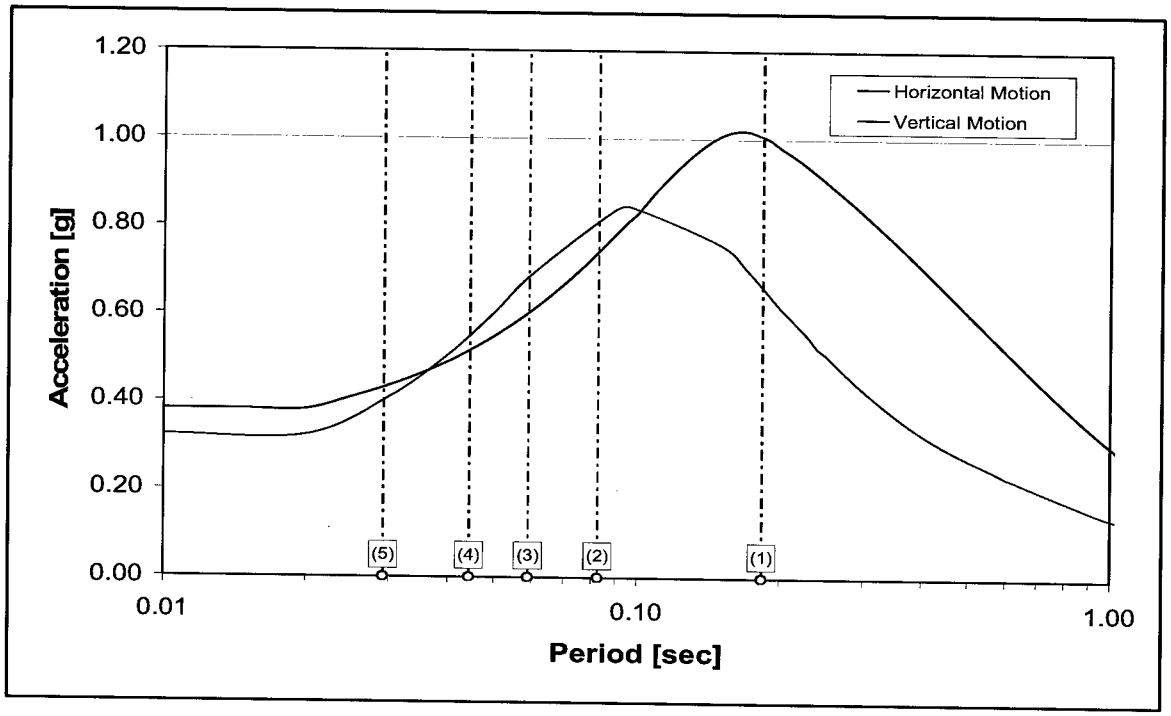

Figure 15. Natural periods and MCE spectra – monolith 21 with flexible foundation

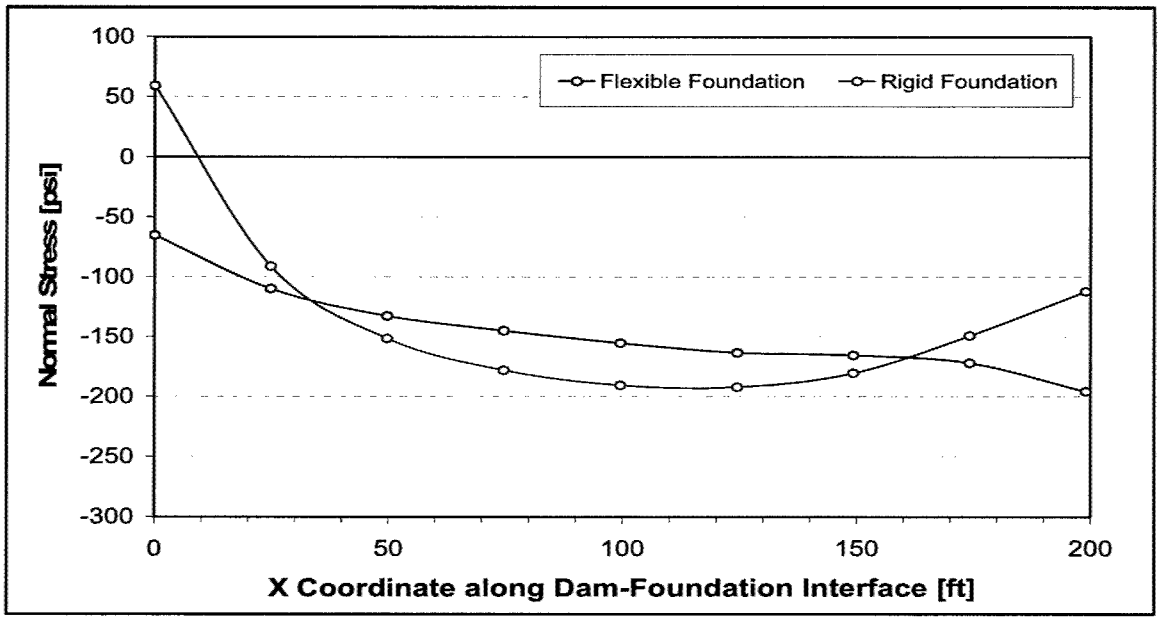

Figure 16. Static normal stress distribution along dam-foundation interface – monolith 21

is depicted by the contour plots shown in Figures 17 and 18, for rigid and flexible foundation conditions, respectively.

Since the structure is not symmetric, the dynamic stresses along the upstream and downstream faces depend on the sign convention used to scale the ground acceleration records. To identify the critical loading scenario, several analyses were performed for each earthquake, combining the initial static loading with each of the two possible directions of the horizontal ([+H], [-H]) and vertical ([+V], [-V]) components. This resulted in four cases for each earthquake: [+H+V], [+H-V], [-H+V], and [-H-V]. A total of 12 different cases were obtained when these combinations of horizontal and vertical components were considered for each one of the three earthquakes. Furthermore, to investigate the influence of the vertical component of the seismic input, dynamic stress analyses were performed considering only the horizontal component of each ground motion. Considering the two possible directions for the horizontal component of each earthquake, this resulted in six additional ground motion cases. Since the damage to a concrete gravity section is essentially associated with the development of tensile stresses, the critical loading scenario for each earthquake was identified as the combination that generated the highest tensile stress value in the section.

Tables 8, 9, and 10 summarize some of the results from the dynamic stress analyses of monolith 21. For each earthquake, the tables show the peak values of maximum principal stresses, their location, and time of occurrence. The stress values represent total stresses as they include the static loading effects. The purpose of Tables 8 through 10 is to identify the critical component combination. The reported principal stress values are element centroidal stresses and therefore their location corresponds to the centroid of the corresponding element. Additional post-processing was performed in the output data to generate the nodal stress values used in the contour plots shown later.

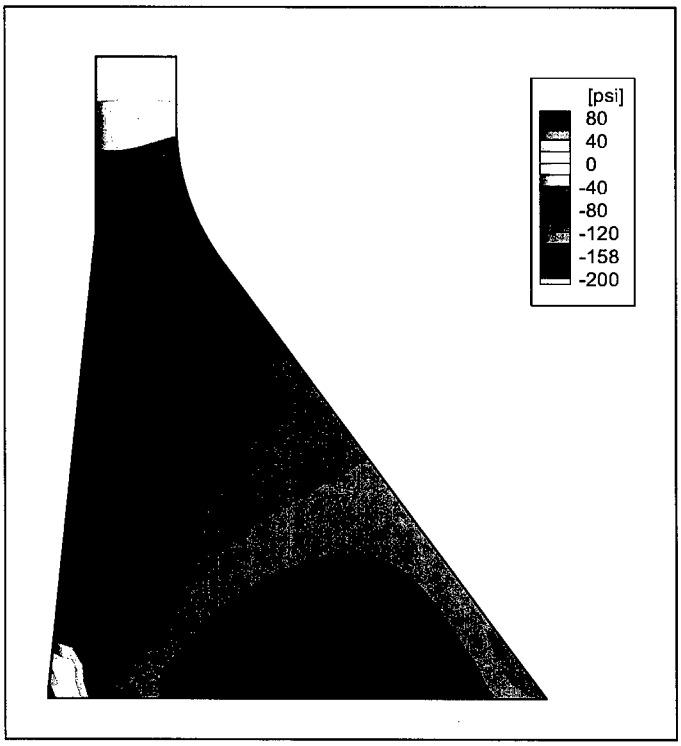

Figure 17. Static stress S_y – monolith 21 with rigid foundation

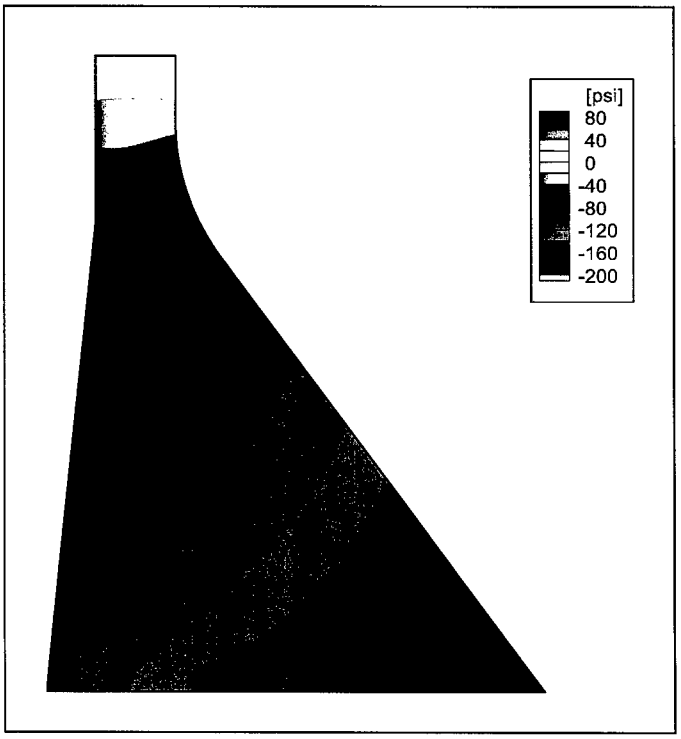

Figure 18. Static stress S_y – monolith 21 with flexible foundation

Table 8
Peak Values of Maximum Principal Stresses – Monolith 21 – San Fernando Earthquake

Case	Location	X (ft)	Y (ft)	Time (sec)	σ_{max} Foundation (psi)
+H	Base (Heel)	4.85	8.75	7.8	603
+H	Upstream	20.53	196.31	3.4	581
+H	Downstream	61.87	196.31	7.9	604
-H	Base (Heel)	4.85	8.75	3.5	606
-H	Upstream	20.53	196.31	7.9	597
-H	Downstream	63.64	192.92	3.4	593
+H+V	Base (Heel)	4.85	8.75	8.5	571
+H+V	Upstream	20.53	196.31	3.4	613
+H+V	Downstream	61.87	196.31	5.4	598
+H-V	Base (Heel)	4.85	8.75	7.8	757
+H-V	Upstream	20.53	196.31	3.9	666
+H-V	Downstream	63.64	192.92	7.9	641
-H+V	Base (Heel)	4.85	8.75	3.5	717
-H+V	Upstream	20.53	196.31	7.9	623
-H+V	Downstream	61.87	196.31	3.9	674
-H-V	Base (Heel)	4.85	8.75	5.4	618
-H-V	Upstream	20.53	196.31	7.9	579
-H-V	Downstream	60.45	199.25	5.5	616

Table 9
Peak Values of Maximum Principal Stresses – Monolith 21 – Imperial Valley Earthquake

Case	Location	X [ft]	Y [ft]	Time [sec]	σ_{max} Foundation [psi]
+H	Base (Heel)	4.85	8.75	19.6	633
+H	Upstream	20.53	196.31	21.7	477
+H	Downstream	61.87	196.31	21.8	504
-H	Base (Heel)	4.85	8.75	24.7	568
-H	Upstream	20.53	196.31	21.8	513
-H	Downstream	63.64	192.92	21.7	492
+H+V	Base (Heel)	4.85	8.75	19.6	704
+H+V	Upstream	20.53	196.31	22.2	674
+H+V	Downstream	63.64	192.92	12.2	723
+H-V	Base (Heel)	4.85	8.75	21.7	661
+H-V	Upstream	20.53	196.31	15.3	598
+H-V	Downstream	63.64	192.92	15.2	524
-H+V	Base (Heel)	4.85	8.75	5.9	616
-H+V	Upstream	20.53	196.31	21.8	499
-H+V	Downstream	61.87	196.31	15.3	575
-H-V	Base (Heel)	4.85	8.75	22.1	737
-H-V	Upstream	20.53	196.31	12.2	705
-H-V	Downstream	61.87	196.31	22.2	691

Table 10
Peak Values of Maximum Principal Stresses – Monolith 21 – Chalfant Earthquake

Case	Location	X [ft]	Y [ft]	Time [sec]	σ_{max} Foundation [psi]
+H	Base (Heel)	4.85	8.75	6.0	699
+H	Upstream	20.53	196.31	7.0	558
+H	Downstream	61.87	196.31	2.7	645
-H	Base (Heel)	4.85	8.75	2.7	629
-H	Upstream	20.53	196.31	2.7	635
-H	Downstream	61.87	196.31	7.0	562
+H+V	Base (Heel)	4.85	8.75	6.0	749
+H+V	Upstream	20.53	196.31	10.0	558
+H+V	Downstream	61.87	196.31	2.7	719
+H-V	Base (Heel)	4.85	8.75	6.0	665
+H-V	Upstream	20.53	196.31	7.0	682
+H-V	Downstream	61.87	196.31	2.7	584
-H+V	Base (Heel)	4.85	8.75	2.7	602
-H+V	Upstream	20.53	196.31	2.7	596
-H+V	Downstream	61.87	196.31	7.0	678
-H-V	Base (Heel)	4.85	8.75	2.7	656
-H-V	Upstream	20.53	196.31	2.7	678
-H-V	Downstream	60.45	199.25	7.0	563

For a given earthquake, three different stress values are reported for each combination of components, and they are the peak centroidal stresses along the base, along the upstream face, and along the downstream face. For the San Fernando earthquake (Table 8), the peak stress value was found at the heel of the dam and it reached a value of 757 psi for the case [+H-V]. This stress value corresponds to the center of the corner element at the heel of the dam, located at 4.85 ft from the upstream face and 8.75 ft above the base. Although this corner region exhibits the highest tensile stresses in the section, the corresponding stress gradient varies very rapidly and the values are significantly reduced towards the interior of the section. The same component combination generated the highest tensile stress (666 psi) along the upstream face, at a location 196 ft above the base. The highest tensile stress along the downstream face was found for the case [–H+V] and it reached 674 psi, at a location 196 ft above the face near the change of slope. The results for the Imperial Valley earthquake (Table 9) indicated a lower tensile stress at the heel (737 psi), but higher peak stresses along both downstream and upstream faces (723 and 705 psi, respectively) when compared to the previous results obtained for the San Fernando earthquake. The peak stresses at the heel and along the upstream face occurred for the case [-H-V], whereas the peak stress along the downstream face corresponded to the case [+H+V]. Another significant difference with respect to the previous case is given by the times of occurrence, since the peak values occurred much later into the analyses. The results for the Chalfant earthquake (Table 10) revealed a peak tensile stress at the heel of 749 psi for the case [+H+V]. The critical tensile

stresses along the downstream and upstream faces reached 719 psi (case [+H+V]) and 682 psi (case [+H-V]), respectively, and they occurred at the same elevations as in the previous cases.

In all three earthquakes, the critical tensile stress conditions were reached for cases involving the combination of both horizontal and vertical ground motion components. The reported peak stresses and their times of occurrence depend on the particular earthquake considered, but in general, the peak values exhibit roughly the same magnitude. The critical combination conditions are controlled in all cases by the stress at the heel and they are given by [+H-V], [-H-V], and [+H+V] for the San Fernando, Imperial Valley, and Chalfant earthquakes, respectively.

Figures 19 through 21 show the time history variation of the maximum principal (centroidal) stresses at the base, downstream face, and upstream face, respectively, for the critical component combination corresponding to the San Fernando earthquake (case [+H-V]). These principal stress time histories reach peak values of 757, 641, and 666 psi, respectively. In general, the time histories show that the most significant tensile demands clearly occur at isolated instances. Figures 22 through 24 show the time history variation of the maximum principal stresses at the base, downstream face, and upstream face, respectively, for the critical component combination corresponding to the Imperial Valley earthquake (case [-H-V]). These principal stress time histories reach peak values of 737, 691, and 705 psi, respectively. Figures 25 through 27 show similar time histories for the Chalfant earthquake (case [+H+V). The stress histories reach peak values of 745, 719, and 558 psi, respectively. As mentioned before, the maximum principal stress at the base (heel) shows the largest tensile peak within the section for the three ground motions considered.

The distribution of the maximum tensile demands across the section is typically depicted by means of contour plots that indicate the peak values reached by a given stress quantity over the duration of the analysis. Figures 28 through 30 show the contour plots of the maximum values of normal vertical stresses (S_y) for the critical component combination corresponding to the San Fernando, Imperial Valley, and Chalfant earthquakes, respectively. As in the static case, normal vertical stresses were selected for these contour plots to facilitate the comparison with the results from previous studies conducted by the Sacramento District. These contour plots were generated using nodal values of the total normal stresses (that is, including static stresses). To highlight the spatial distribution of tensile demands, the contours were generated using a minimum cutoff value of 150 psi. The peak values of maximum normal vertical stresses across the section are 696 psi (San Fernando [+H-V]), 698 psi (Imperial Valley [-H-V]), and 693 psi (Chalfant [+H+V]).

Figure 31 shows the distribution of maximum normal vertical stresses along the upstream face of the monolith for the San Fernando earthquake (case [+H-V]). To assess the influence of the vertical component of the input ground motion, two different cases are considered: a) horizontal component only, and b) both horizontal and vertical components. In addition, total (S_y, including static effects) and

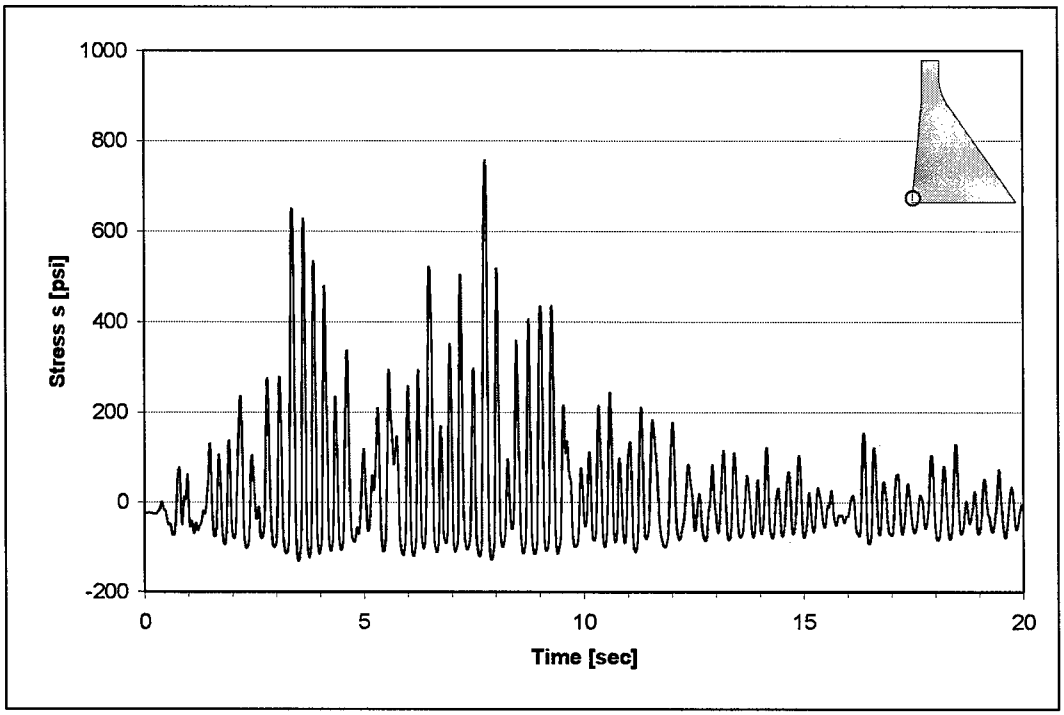

Figure 19. Maximum principal stress – monolith 21 (heel) – San Fernando earthquake [+H-V]

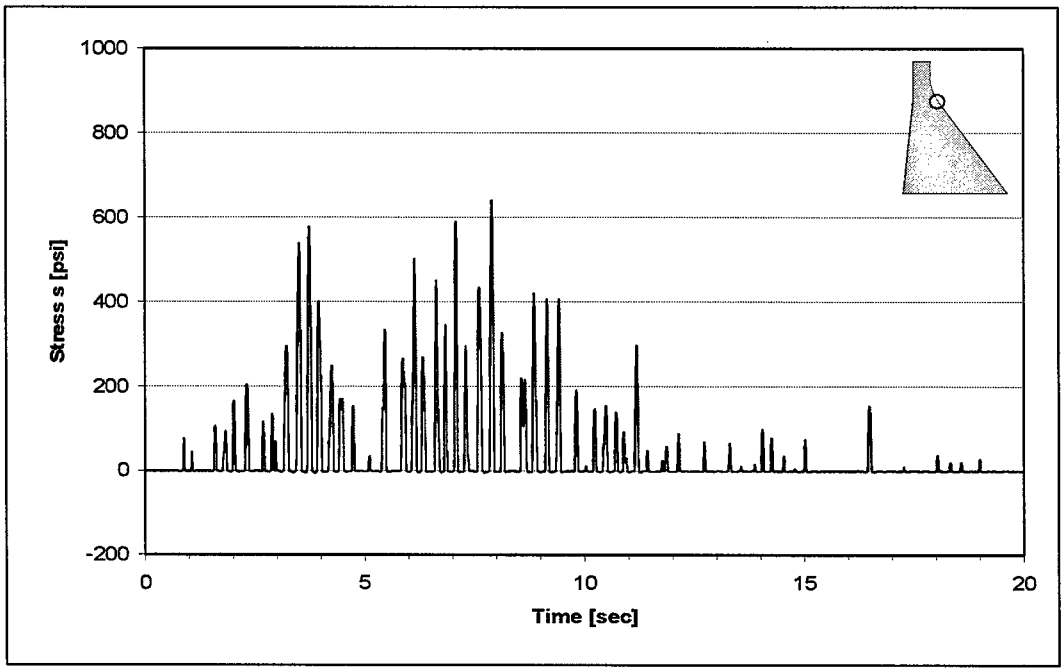

Figure 20. Maximum principal stress – monolith 21 (downstream) – San Fernando earthquake [+H-V]

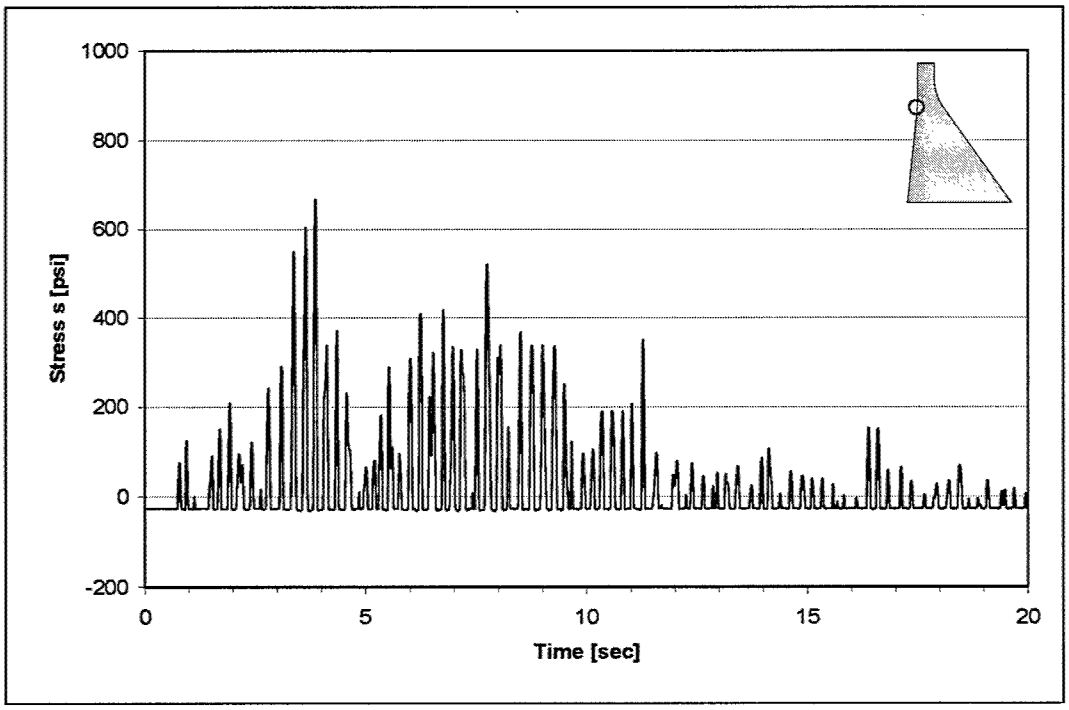

Figure 21. Maximum principal stress – monolith 21 (upstream) – San Fernando earthquake [+H-V]

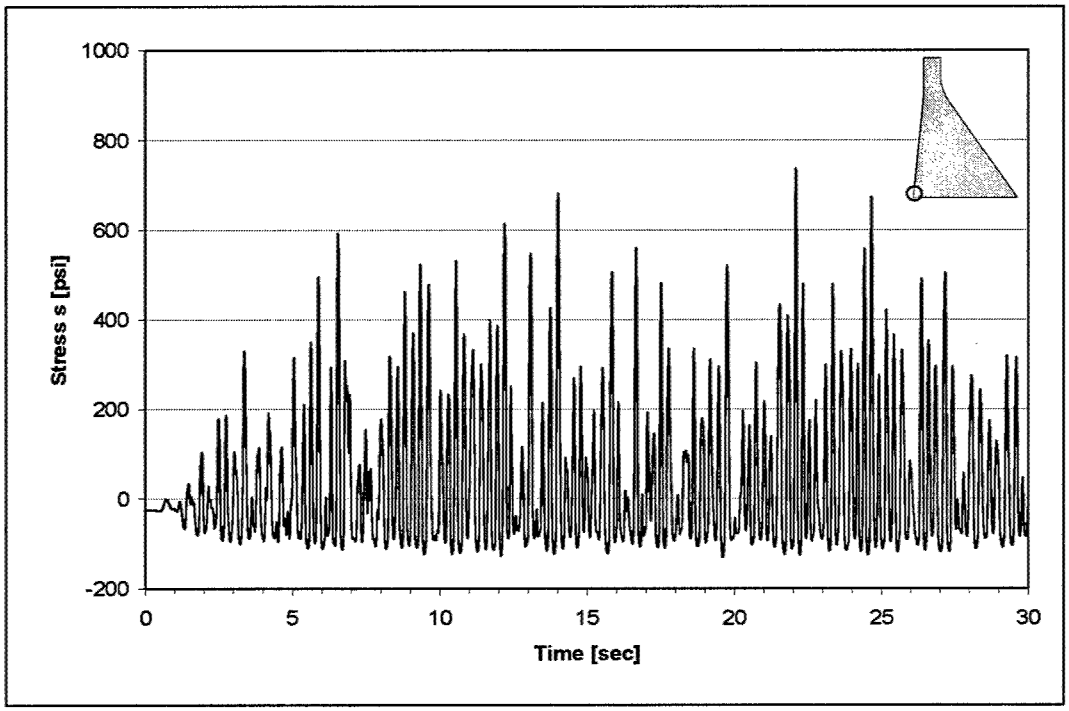

Figure 22. Maximum principal stress – monolith 21 (heel) – Imperial Valley earthquake [-H-V]

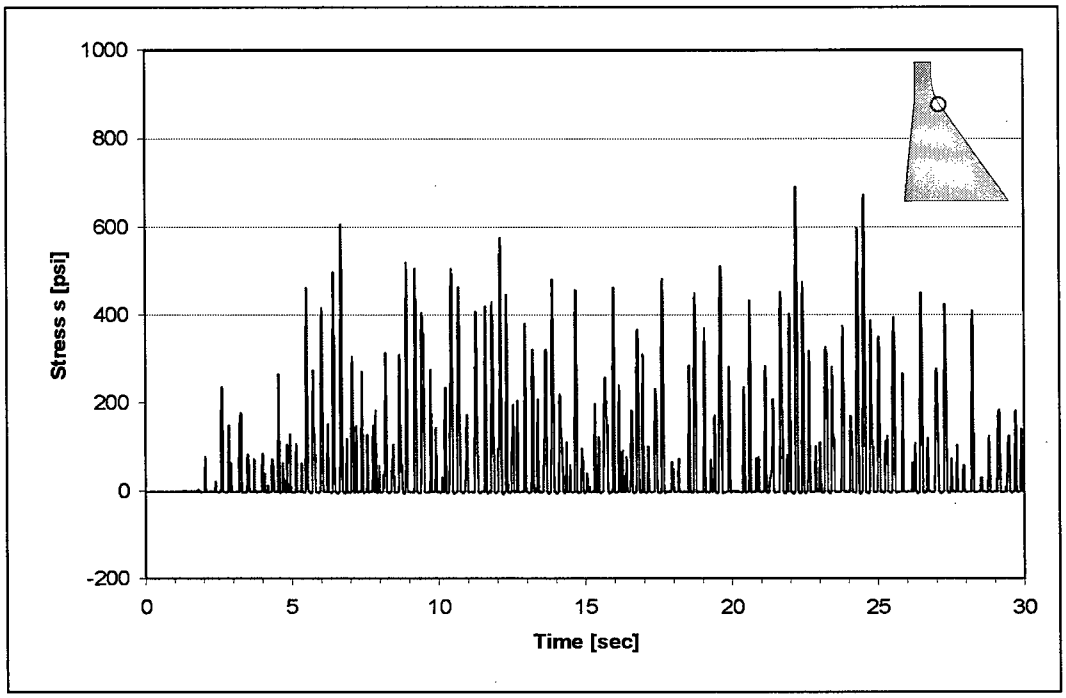

Figure 23. Maximum principal stress – monolith 21 (downstream) – Imperial Valley earthquake [-H-V]

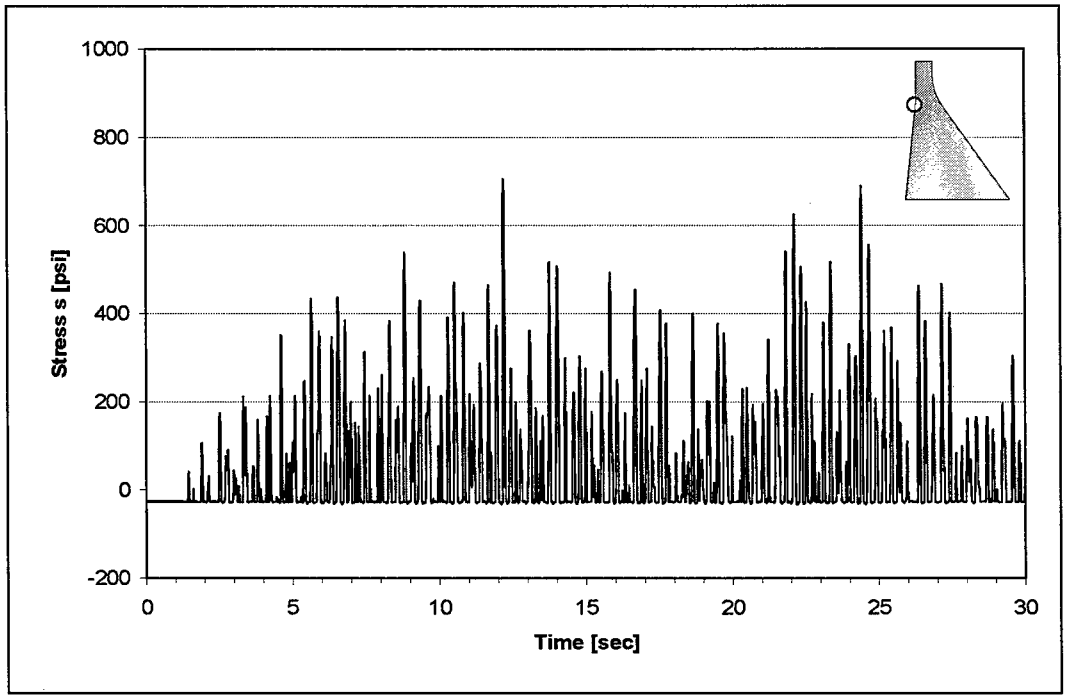

Figure 24. Maximum principal stress – monolith 21 (upstream) – Imperial Valley earthquake [-H-V]

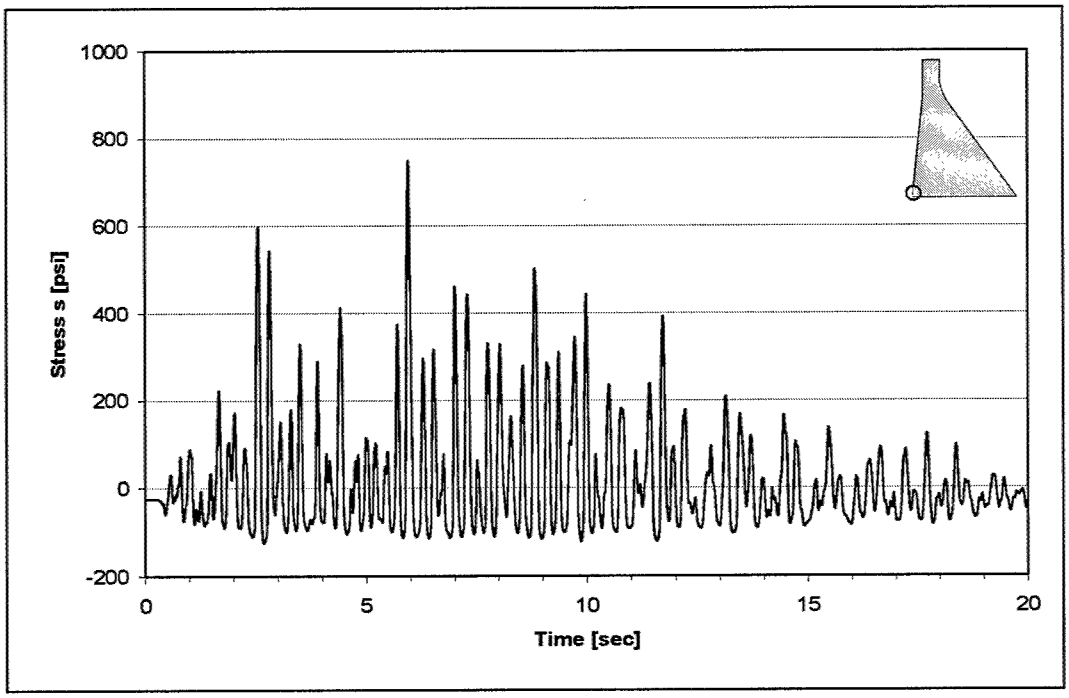

Figure 25. Maximum principal stress – monolith 21 (heel) – Chalfant earthquake [+H+V]

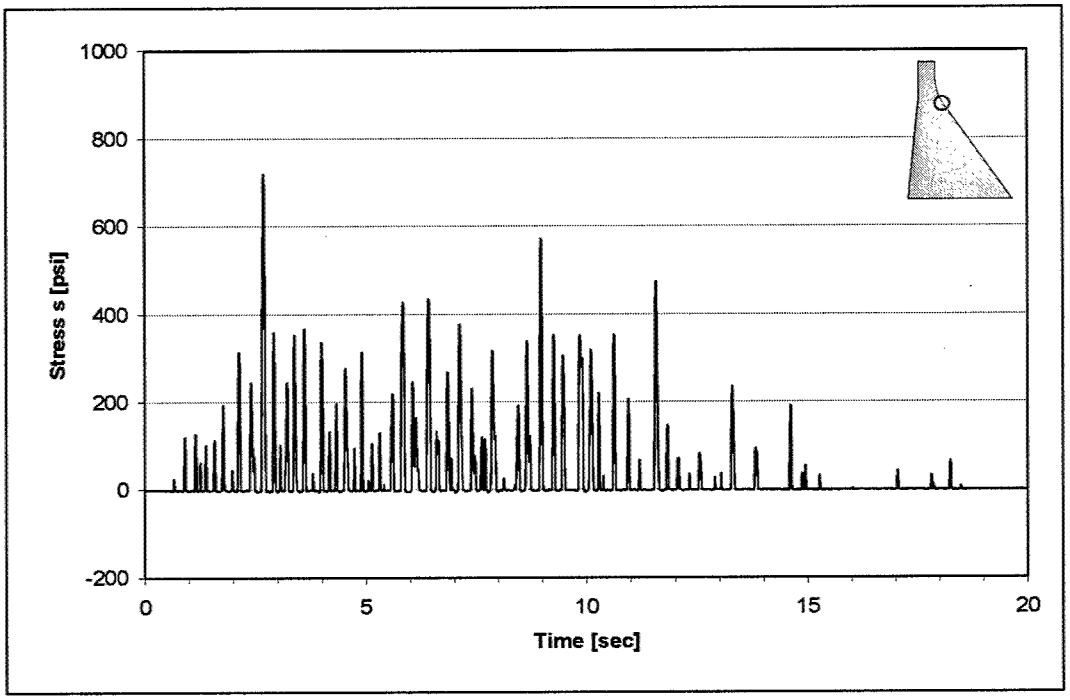

Figure 26. Maximum principal stress – monolith 21 (downstream) – Chalfant earthquake [+H+V]

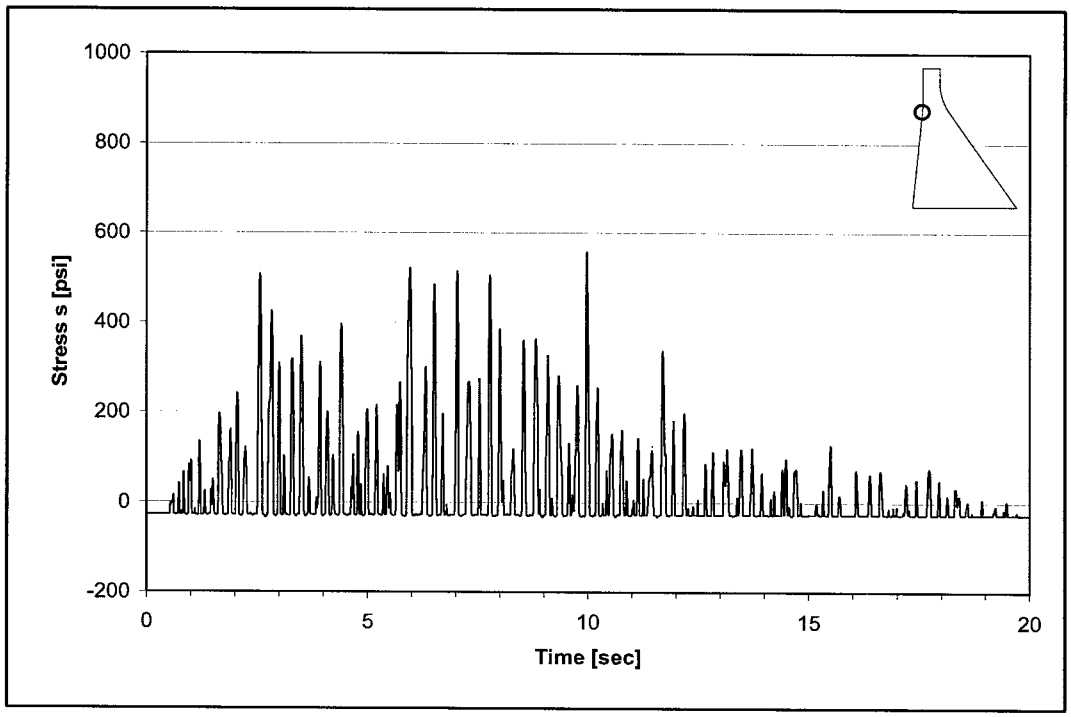

Figure 27. Maximum principal stress – monolith 21 (upstream) – Chalfant earthquake [+H+V]

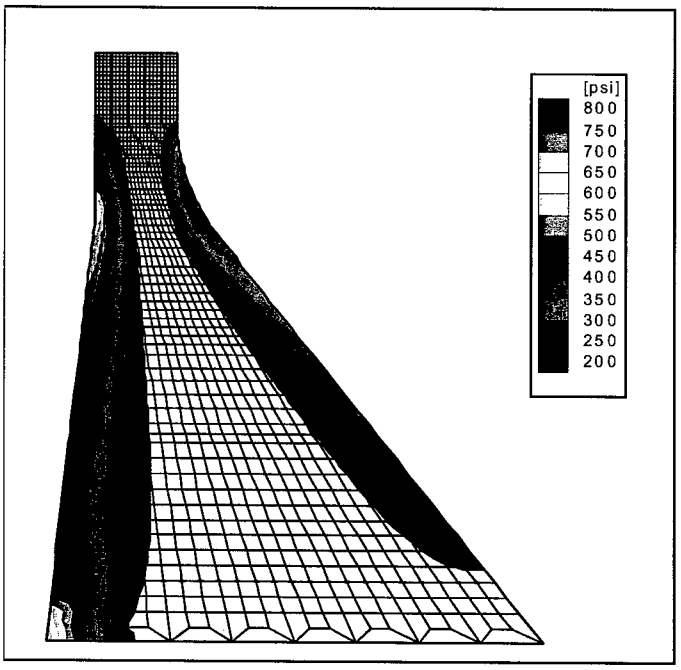

Figure 28. Normal vertical stress S_y – monolith 21 – San Fernando earthquake [+H-V]

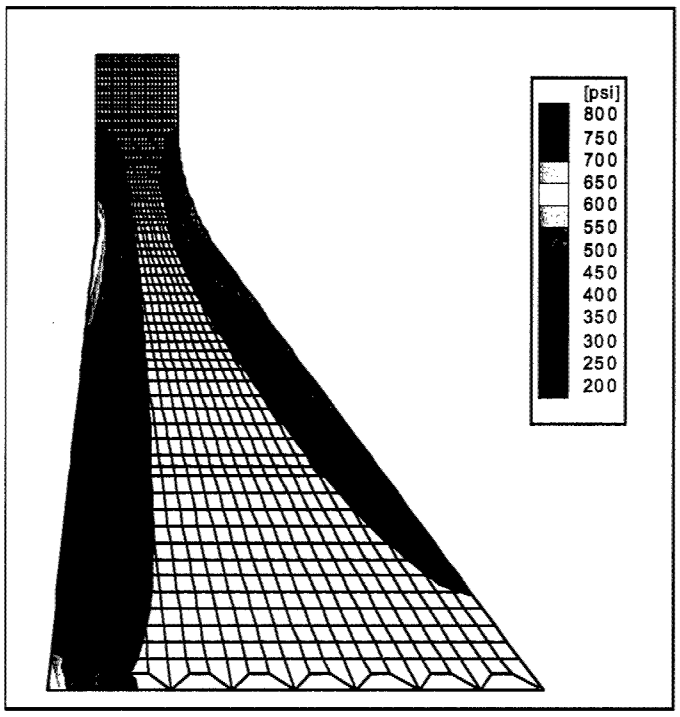

Figure 29. Normal vertical stress S_y – monolith 21 – Imperial Valley earthquake [-H-V]

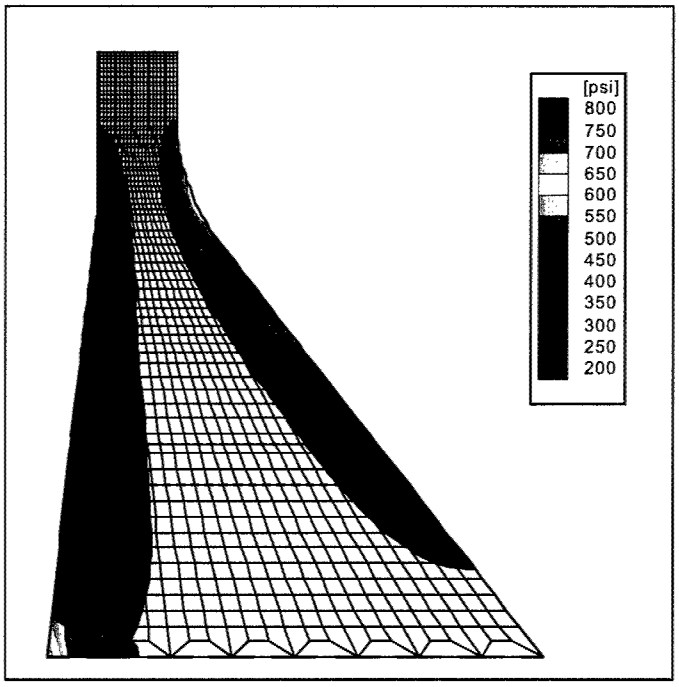

Figure 30. Normal vertical stress S_y – monolith 21 – Chalfant earthquake [+H+V]

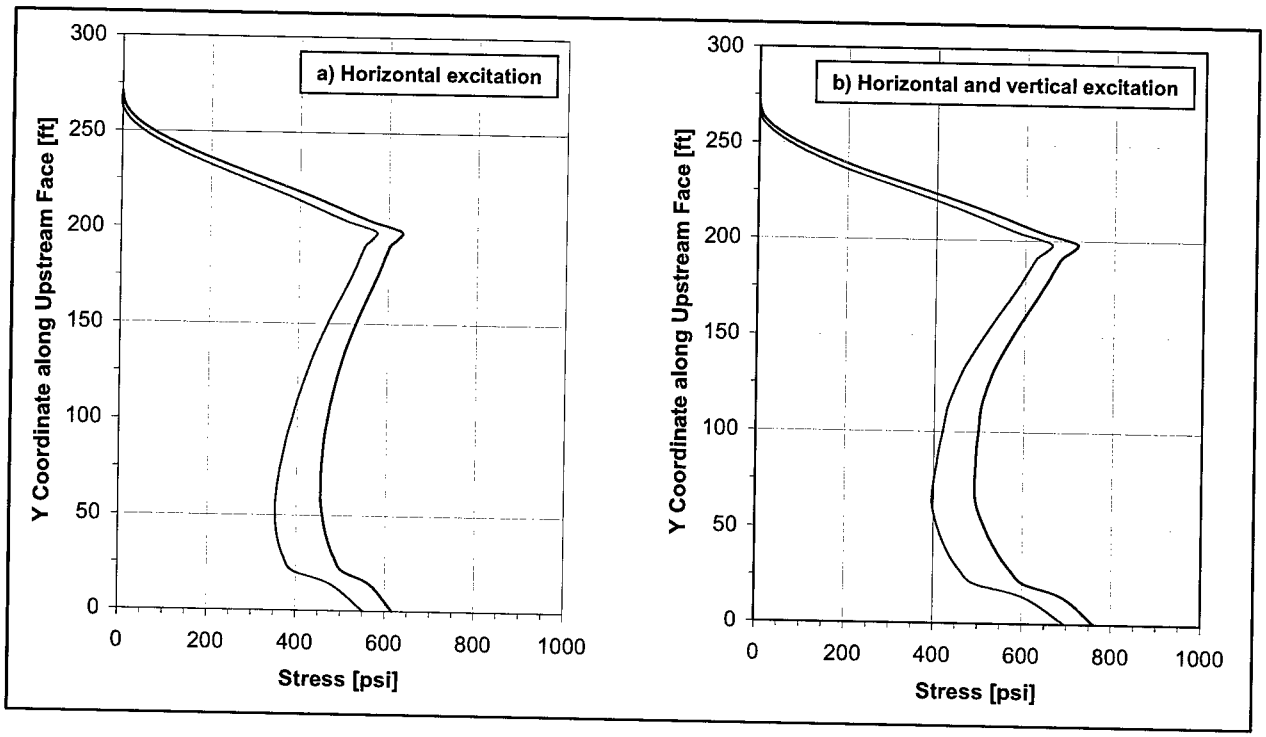

Figure 31. Distribution of maximum total (blue) and dynamic (red) normal vertical stresses along the upstream face of monolith 21 – San Fernando earthquake – cases [+H] and [+H-V]

dynamic (S_y^d, excluding static effects) normal stresses are shown in the figure (blue and red lines, respectively). For the horizontal excitation case, the highest stresses occurred at about 72 percent of the height (S_y = 574 psi, S_y^d = 632 psi). When both ground motion components are considered, the highest stresses occurred at the base (S_y = 696 psi, S_y^d = 761 psi). Figure 32 shows the variation of maximum normal stresses along the upstream face for the Imperial Valley earthquake (case [-H-V]). For the case of horizontal excitation only, the highest stresses occurred at the base (S_y = 519 psi, S_y^d = 584 psi). However, in the case of both horizontal and vertical components, the highest total stress occurred at 72 percent of the height (S_y = 698 psi), but the highest dynamic stress was found at the base (S_y^d = 782 psi). Finally, similar plots depicting the maximum normal stresses along the upstream face for the case of the Chalfant earthquake (case [+H+V]) are shown in Figure 33. The highest normal stresses occurred at the base for both cases "a" (S_y = 640 psi, S_y^d = 706 psi) and "b" (S_y = 693 psi, S_y^d = 758 psi).

Results – monolith 14

As described before, three different finite-element models were initially considered for the middle cross section of monolith 14. The models attempted to account for the presence of the spillway pier and the openings corresponding to

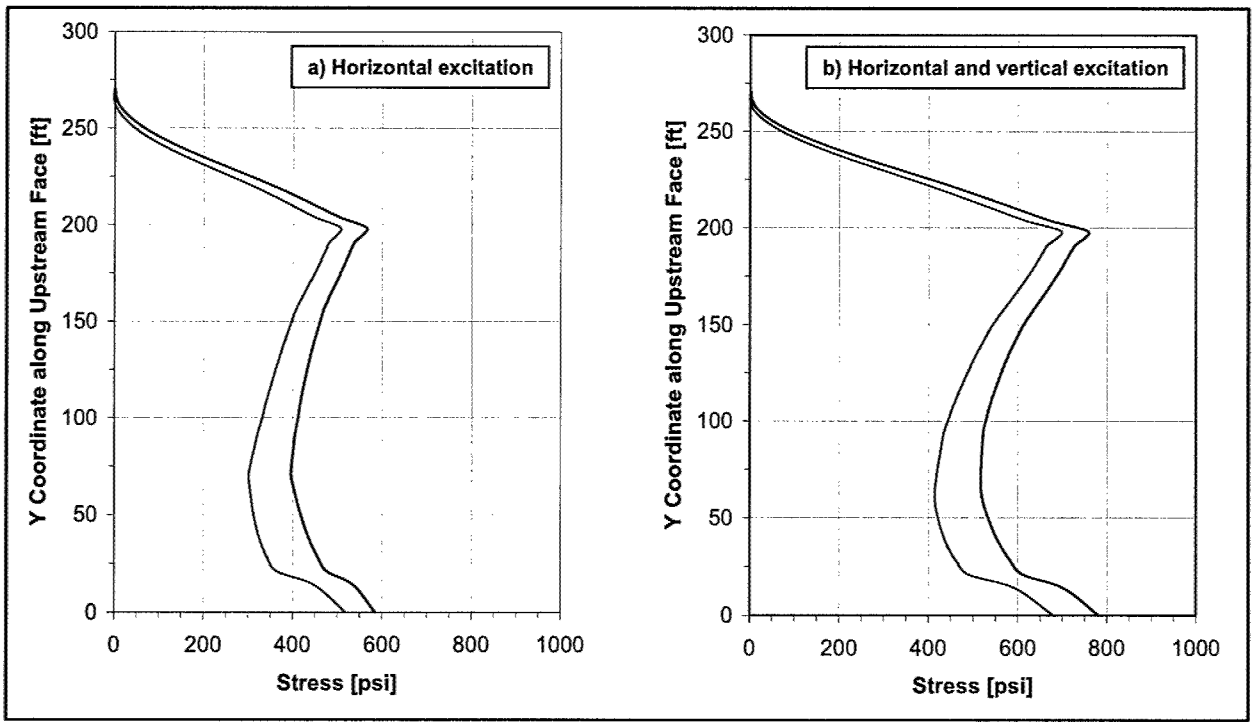

Figure 32. Distribution of maximum total (blue) and dynamic (red) normal vertical stresses along the upstream face of monolith 21 – Imperial Valley earthquake – cases [-H] and [-H-V]

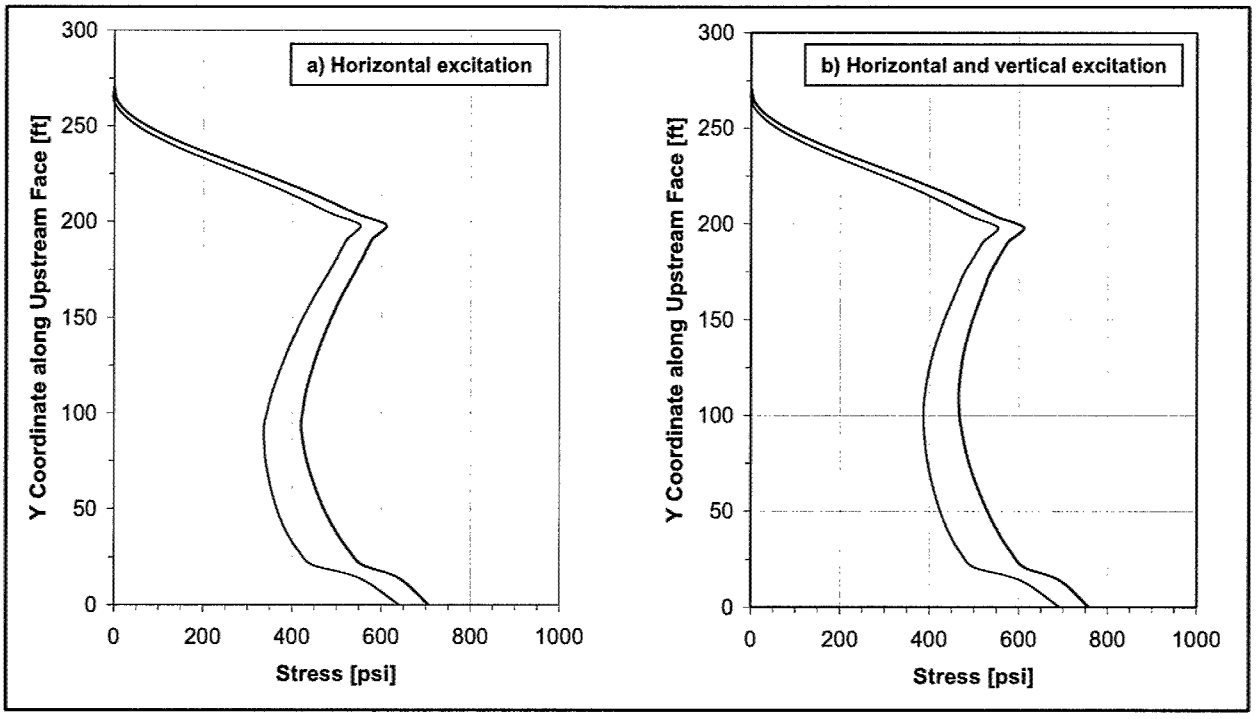

Figure 33. Distribution of maximum total (blue) and dynamic (red) normal vertical stresses along the upstream face of monolith 21 – Chalfant earthquake – cases [+H] and [+H+V]

the chambers and conduits. The first model (Model 1) accounts for the presence of the spillway pier by using equivalent material properties; the second model (Model 2) represents the spillway pier, both chambers, and both conduits by means of equivalent material properties; and the third model (Model 3) uses equivalent material properties to represent the spillway pier and the conduits but it incorporates the voids corresponding to the chambers. The motivation was to capture—at least globally—the effects of those features on the overall dynamic characteristics of the system. The proper evaluation of the state of stress and deformation near those features obviously requires three-dimensional modeling. However, it was expected that these approximate models would be able to generate reasonable estimates of the overall level of stress demands across the section of the monolith.

Tables 11 and 12 show the first ten natural frequencies corresponding to the three models of monolith 14 for empty reservoir conditions. Table 11 corresponds to the rigid foundation case ($E_f = \infty$), and Table 12 corresponds to the flexible foundation case ($E_f = 7.9 \bullet 10^6$ psi). Depending on the model, the incorporation of foundation flexibility causes an increase of about 35 to approximately 39 percent in the fundamental period of the dam-foundation system with respect to the dam on rigid base. In general, foundation flexibility increases all the natural periods, with a higher influence on the period corresponding to the second vibration mode.

Table 11
Natural Frequencies – Monolith 14 with Rigid Foundation (Empty Reservoir)

Mode	Rigid Foundation (1)		Rigid Foundation (2)		Rigid Foundation (3)	
	Frequency (Hz)	Period (sec)	Frequency (Hz)	Period (sec)	Frequency (Hz)	Period (sec)
1	6.26	0.160	6.16	0.162	6.06	0.165
2	14.17	0.071	14.09	0.071	13.68	0.073
3	15.07	0.066	14.97	0.067	14.80	0.068
4	22.90	0.044	22.91	0.044	22.20	0.045
5	31.62	0.032	31.60	0.032	30.13	0.033
6	33.69	0.030	33.67	0.030	32.34	0.031
7	37.58	0.027	37.57	0.027	34.92	0.029
8	39.81	0.025	39.79	0.025	36.58	0.027
9	43.01	0.023	43.01	0.023	40.16	0.025
10	45.98	0.022	45.75	0.022	40.98	0.024

Based on the objectives of the analyses, Model 2 was adopted as the most appropriate representation of the monolith section. This model incorporates the appropriate modifications in the material properties to reflect the presence of the spillway pier, the chambers, and the conduits, while assuming an idealized 2D section of uniform thickness. Although in a simplified manner, this model accounts for the chambers and the conduits, and therefore it is likely to generate a better approximation of the actual dynamic response characteristics of the structure than Model 1 (which considers only the influence of the spillway pier). On

Table 12
Natural Frequencies – Monolith 14 with Flexible Foundation (Empty Reservoir)

Mode	Flex. Foundation (1)		Flex. Foundation (2)		Flex. Foundation (3)	
	Frequency (Hz)	Period (sec)	Frequency (Hz)	Period (sec)	Frequency (Hz)	Period (sec)
1	4.50	0.222	4.51	0.222	4.50	0.222
2	7.21	0.139	7.31	0.137	7.36	0.136
3	10.23	0.098	10.27	0.097	10.23	0.098
4	18.48	0.054	18.47	0.054	17.84	0.056
5	24.44	0.041	24.03	0.042	22.96	0.044
6	26.47	0.038	26.37	0.038	25.51	0.039
7	32.03	0.031	31.83	0.031	29.48	0.034
8	35.57	0.028	35.61	0.028	33.89	0.030
9	37.53	0.027	37.26	0.027	35.79	0.028
10	39.95	0.025	39.55	0.025	36.10	0.028

the other hand, Model 3 exaggerates the influence of the chamber voids, whose width (in the direction normal to the plane of the section) becomes then equal to the monolith thickness in a 2D representation that assumes a section of uniform thickness. The locations of the first five natural periods of Model 2 are shown in Figures 34 and 35 with respect to the MCE 5-percent-damped horizontal and vertical response spectra. The results in Figures 34 and 35 correspond to rigid and flexible foundations, respectively, and they were computed for empty reservoir conditions.

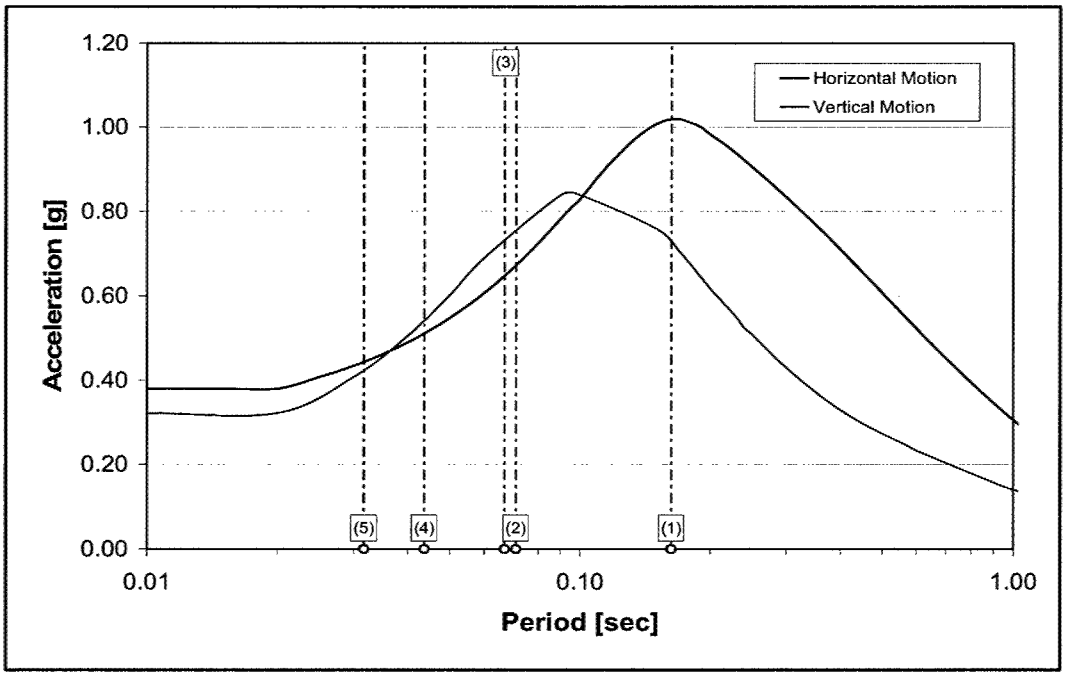

Figure 34. Natural periods and MCE spectra – monolith 14 with rigid foundation

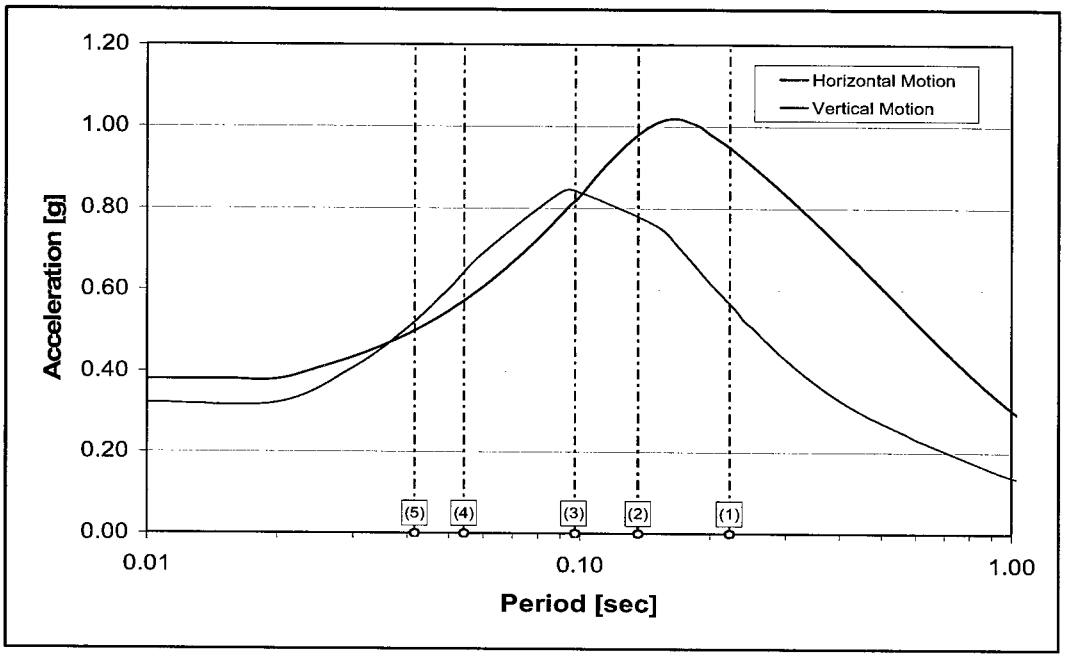

Figure 35. Natural periods and MCE spectra – monolith 14 with flexible foundation

Figure 36 shows the distribution of static normal vertical stress (S_y) along the dam-foundation interface, considering only self-weight and hydrostatic loading. The results, which correspond to Model 2, are presented for both rigid and flexible foundation conditions. The figure shows that for the assumed reservoir level (gross pool elevation at 466 ft), the static normal stress at the heel of the dam reaches values of 115 psi and -48 psi, for rigid and flexible base conditions, respectively. The distribution of the normal vertical stress S_y across the section is depicted by the contour plots shown in Figures 37 and 38, for rigid and flexible foundation cases, respectively.

Tables 13 through 15 indicate the peak values of the maximum principal stresses in the section computed for the San Fernando, Imperial Valley, and Chalfant earthquakes, respectively. The principal stress values reported in these tables correspond to element (centroidal) stresses, and they include the static contributions. For all three earthquakes, the highest tensile stress occurred at the heel of the section. For the San Fernando earthquake, the highest value of maximum principal stress reached 897 psi, which occurred for the [+H-V] component combination. The results corresponding to the Imperial Valley and Chalfant earthquakes indicated values of maximum principal stresses up to 790 psi (case [-H-V]) and 746 psi (case [+H+V]), respectively. The three critical component combinations coincide with those identified for the seismic demand at the base of monolith 21.

Solely examining the peak stress responses at selected locations does not provide sufficient information to judge the comparative severity of different ground motions, and a thorough evaluation of the seismic performance of a concrete dam must take into account not only the magnitude of the stress responses but also their time-varying characteristics. The time histories of the critical maximum

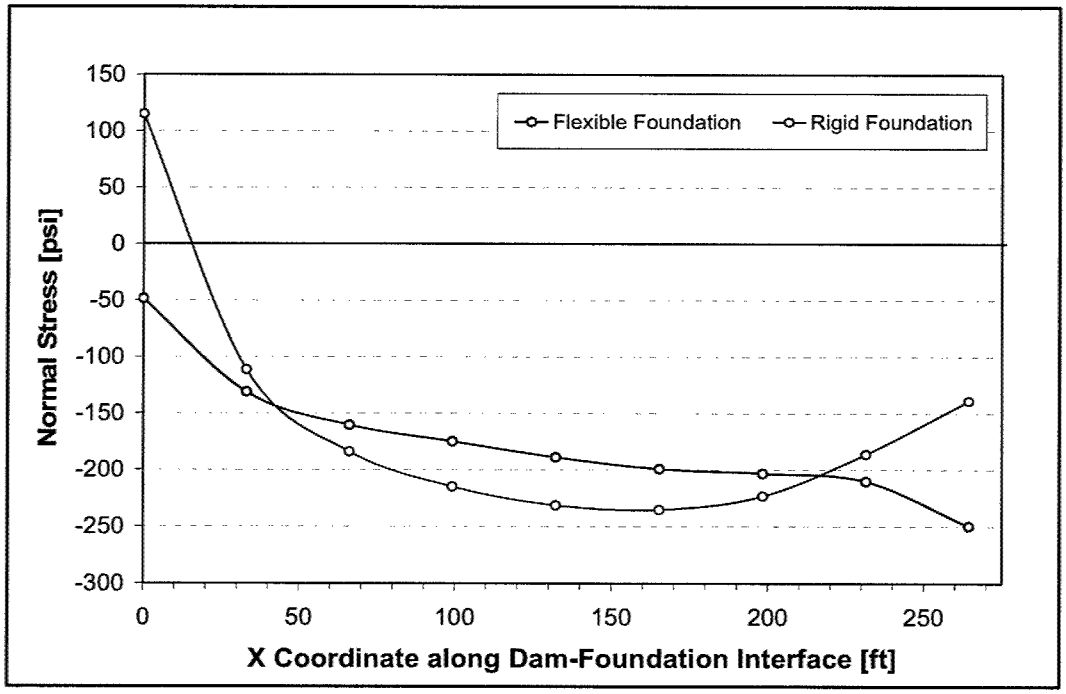

Figure 36. Static normal stress distribution along dam-foundation interface – monolith 14

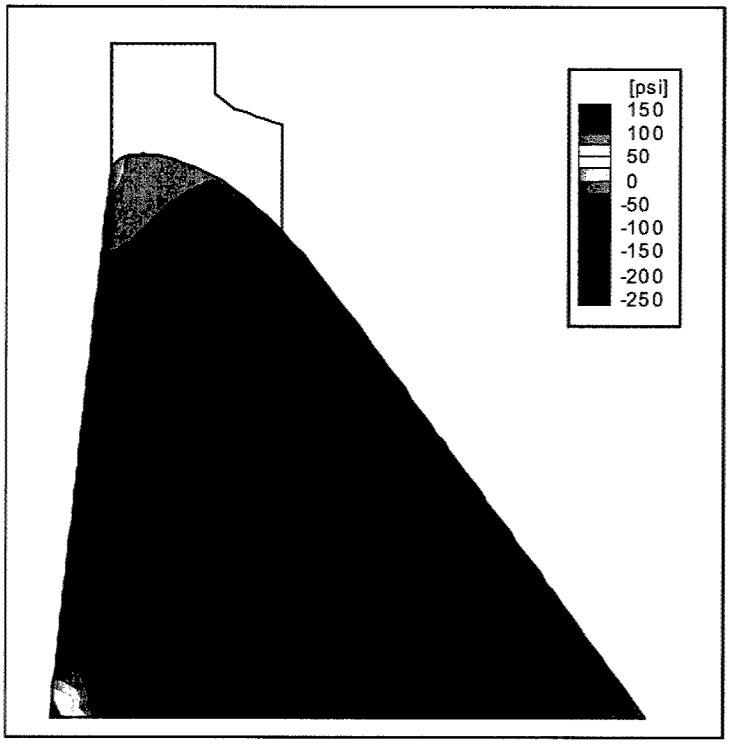

Figure 37. Static stress S_y – monolith 14 with rigid foundation

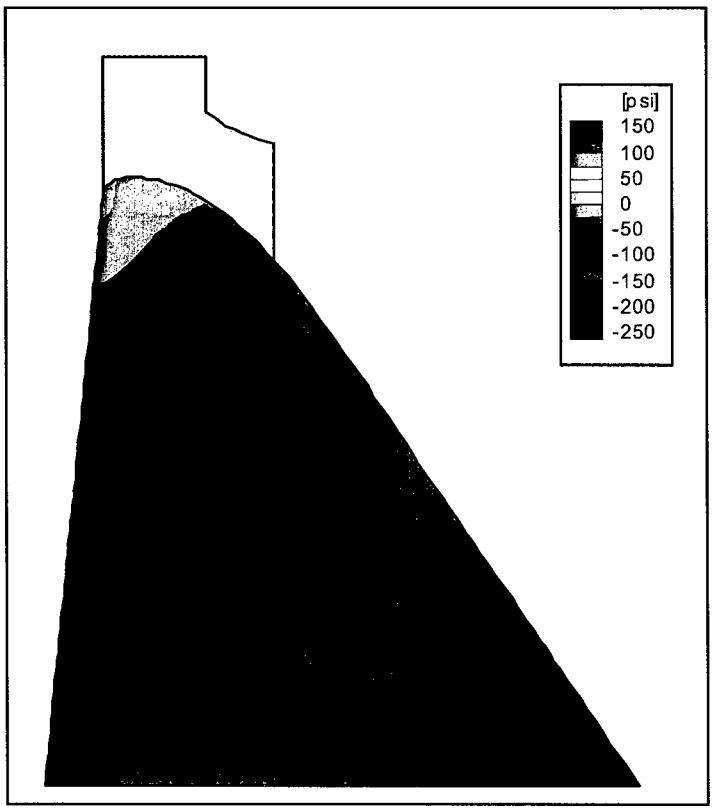

Figure 38. Static stress S_y – monolith 14 with flexible foundation

Table 13
Peak Values of Maximum Principal Stresses – Monolith 14 – San Fernando Earthquake

Case	Location	X (ft)	Y (ft)	Time (sec)	σ_{max} Foundation (psi)
+H	Base (Heel)	6.01	6.07	7.8	715
-H	Base (Heel)	6.01	6.07	5.9	594
+H+V	Base (Heel)	6.01	6.07	8.5	685
+H-V	Base (Heel)	6.01	6.07	7.8	897
-H+V	Base (Heel)	6.01	6.07	7.9	741
-H-V	Base (Heel)	6.01	6.07	5.4	745

Table 14
Peak Values of Maximum Principal Stresses – Monolith 14 – Imperial Valley Earthquake

Case	Location	X (ft)	Y (ft)	Time (sec)	σ_{max} Foundation (psi)
+H	Base (Heel)	6.01	6.07	15.7	722
-H	Base (Heel)	6.01	6.07	14.1	648
+H+V	Base (Heel)	6.01	6.07	15.7	707
+H-V	Base (Heel)	6.01	6.07	15.7	736
-H+V	Base (Heel)	6.01	6.07	6.6	604
-H-V	Base (Heel)	6.01	6.07	14.1	790

Table 15
Peak Values of Maximum Principal Stresses – Monolith 14 – Chalfant Earthquake

Case	Location	X (ft)	Y (ft)	Time (sec)	σ_{max} Foundation (psi)
+H	Base (Heel)	6.01	6.07	9.7	659
-H	Base (Heel)	6.01	6.07	9.9	693
+H+V	Base (Heel)	6.01	6.07	6.0	746
+H-V	Base (Heel)	6.01	6.07	9.7	682
-H+V	Base (Heel)	6.01	6.07	11.6	689
-H-V	Base (Heel)	6.01	6.07	9.9	739

principal stresses are presented in Figures 39 through 41 for the three earthquakes. As mentioned before, the San Fernando case shows the most significant tensile peak (897 psi), but high values appear as isolated tensile excursions (for example, the maximum principal stress history exceeds 700 psi only twice).

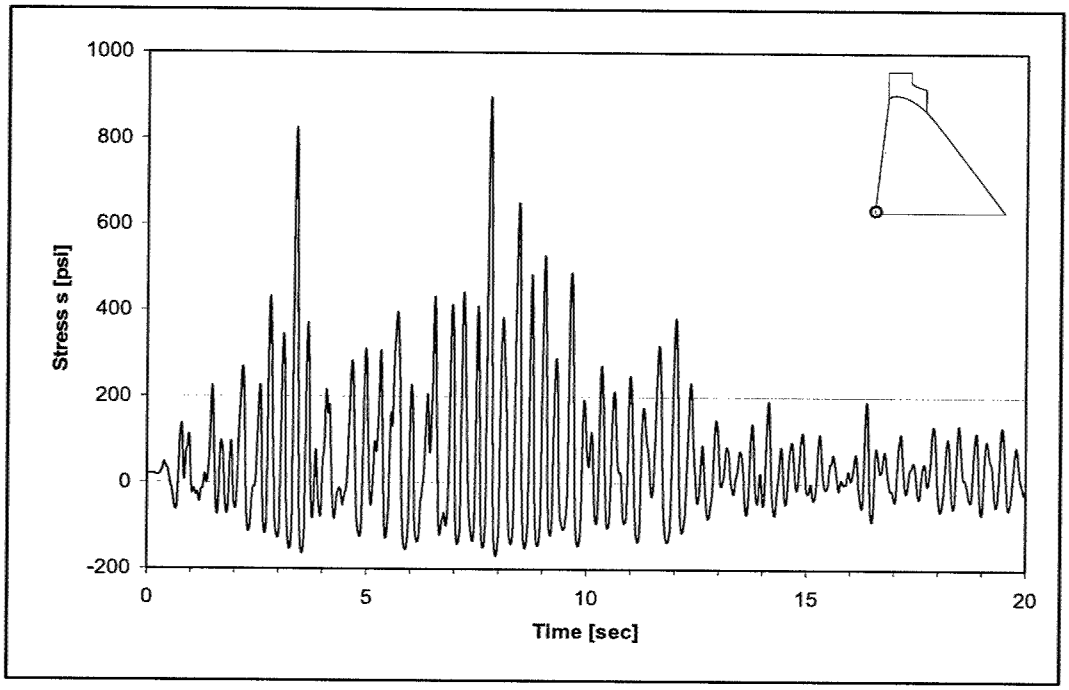

Figure 39. Maximum principal stress – monolith 14 (heel) – San Fernando earthquake [+H-V]

It is also important to evaluate the spatial distribution of the tensile demands across the section. Contour plots of the peak values of normal vertical stresses (S_y) are shown in Figures 42 through 44 for the critical component combinations corresponding to the San Fernando, Imperial Valley, and Chalfant earthquakes, respectively. This particular response quantity was selected to facilitate the comparison with the results from the previous response-spectrum-based seismic analyses performed by the Sacramento District. The stress contours were generated using nodal normal stress values that included the effects of the static loads. Only

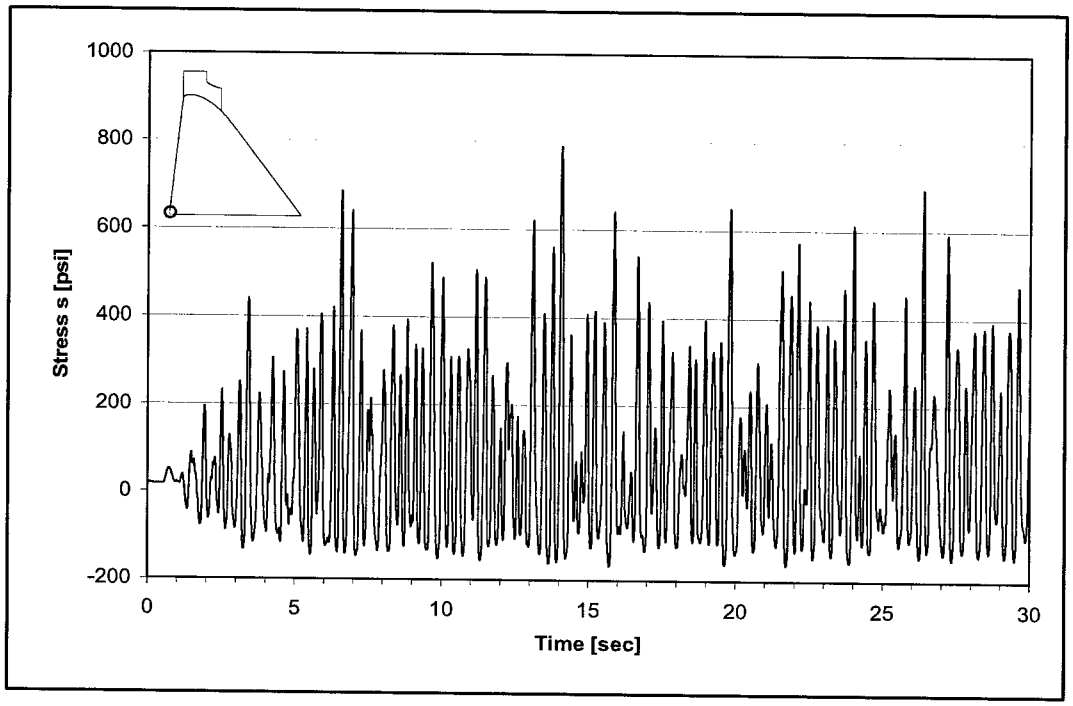

Figure 40. Maximum principal stress – monolith 14 (heel) – Imperial Valley earthquake [-H-V]

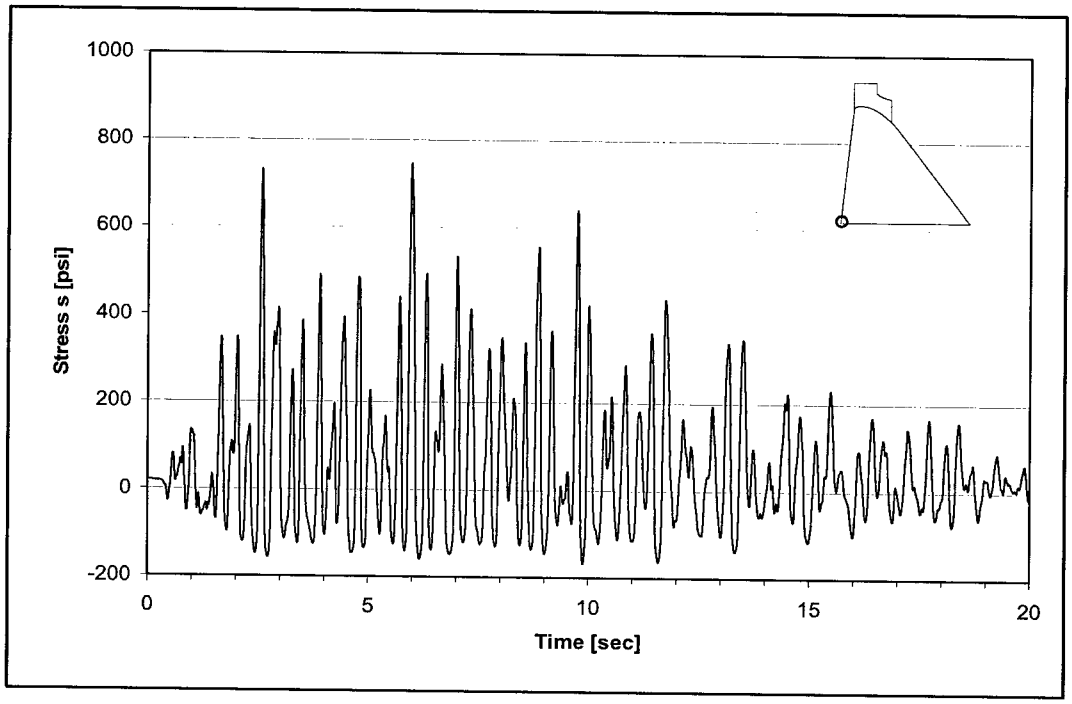

Figure 41. Maximum principal stress – monolith 14 (heel) – Chalfant earthquake [+H+V]

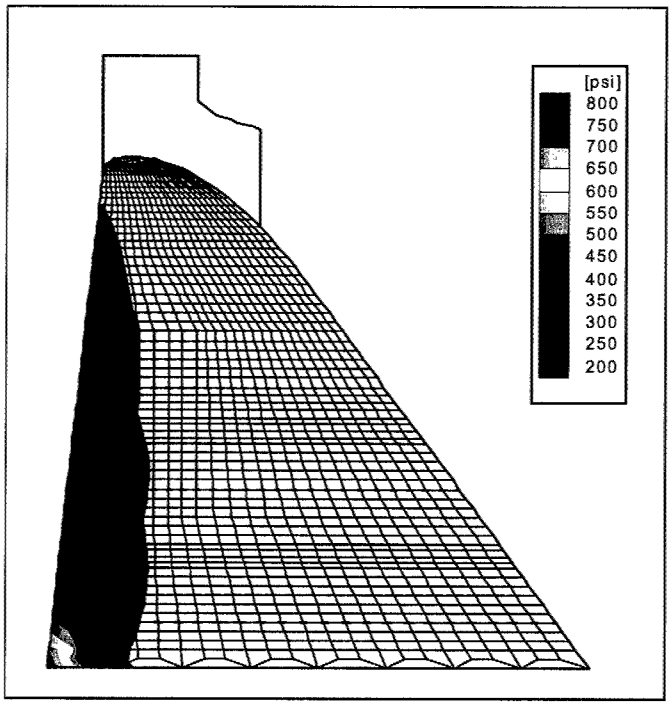

Figure 42. Normal vertical stress S_y – monolith 14 – San Fernando earthquake [+H-V]

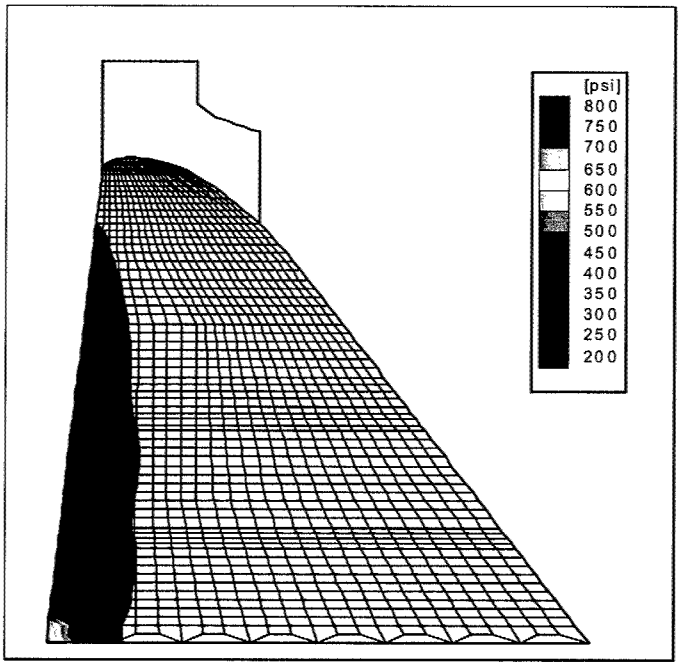

Figure 43. Normal vertical stress S_y – monolith 14 – Imperial Valley earthquake [-H-V]

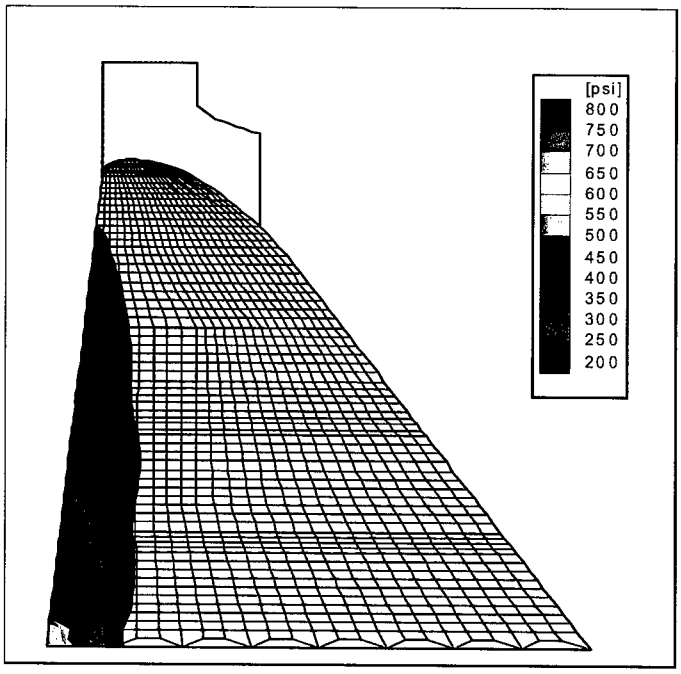

Figure 44. Normal vertical stress S_y – monolith 14 – Chalfant earthquake [+H+V]

tensile demands exceeding 150 psi are presented in the figures. The normal vertical stresses across the section reach peak positive values of 789, 693, and 650 psi for the San Fernando (case [+H-V]), Imperial Valley (case [-H-V]), and Chalfant (case [+H+V]) earthquakes, respectively. In all cases, the peak values occurred at the heel of the section.

The influence of the vertical component of the input ground motion on the stress response is investigated in Figures 45 through 47. They show the peak values of the maximum vertical stresses along the upstream face of the dam section. Each figure shows the stresses due to horizontal excitation (case a) and both ground motion components (case b). Also, the influence of the static stresses on the total response is evaluated by displaying not only the total vertical stresses (S_y), but also the dynamic vertical stresses (S_y^d, excluding static effects). As previously indicated by the contour plots, the highest tensile demands take place at the base for all cases. Figure 45 shows the profile of vertical stresses for the San Fernando earthquake, with peak values of S_y = 789 psi and S_y^d = 838 psi for the case in which both ground motion components act simultaneously. Notice that if only the horizontal component of the earthquake motion is considered, the corresponding peak values are approximately 80 percent (S_y^H = 616 psi and S_y^{Hd} = 665 psi) of those obtained for both excitation components. Figure 46 corresponds to the Imperial Valley earthquake, and it exhibits peak stresses of S_y = 693 psi and S_y^d = 742 psi (both ground motion components). The horizontal excitation case exhibits peak values that are again 80 percent (S_y^H = 555 psi and S_y^{Hd} = 603 psi) of

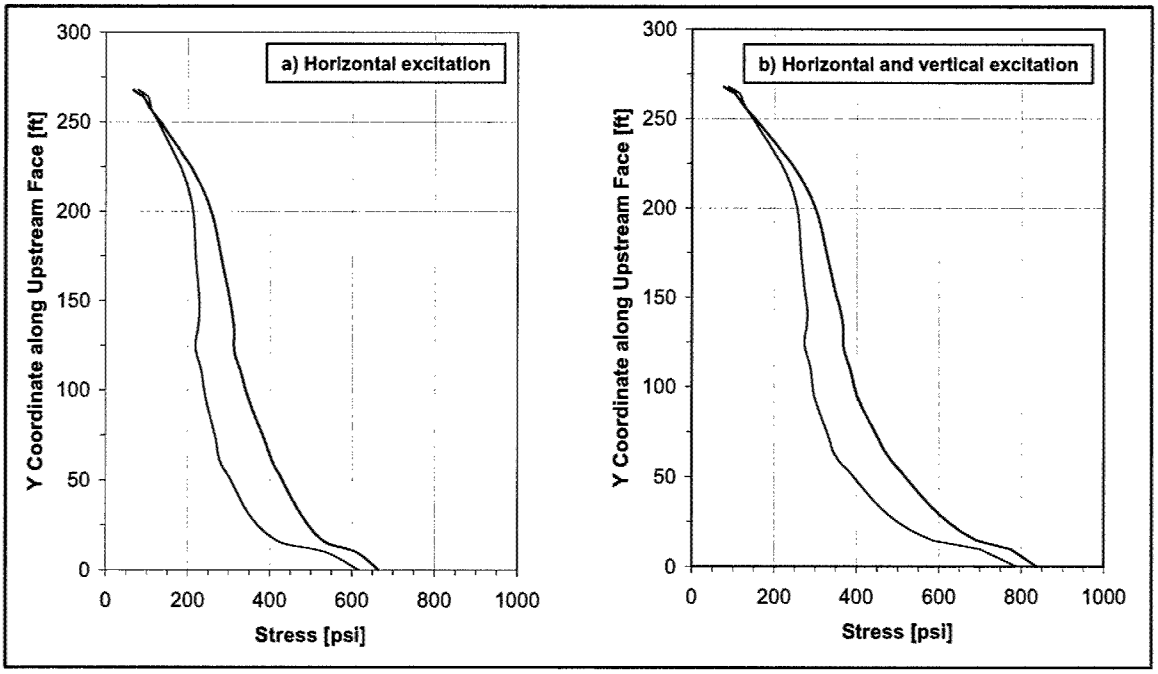

Figure 45. Distribution of maximum total (blue) and dynamic (red) normal vertical stresses along the upstream face of monolith 14 – San Fernando earthquake – cases [+H] and [+H-V]

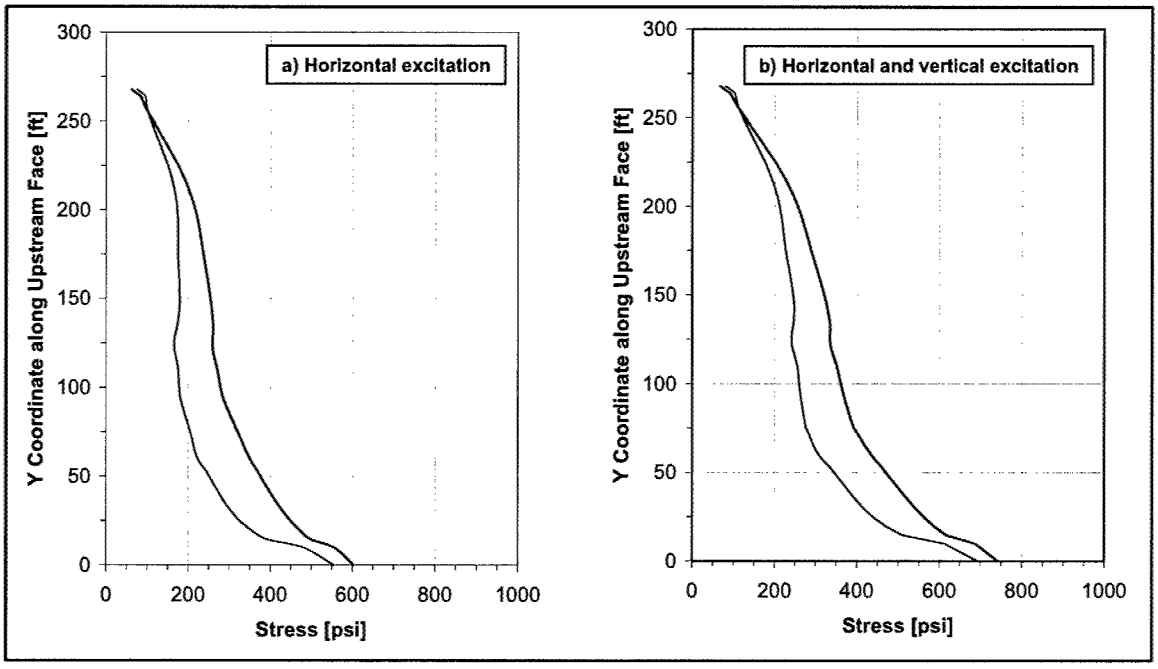

Figure 46. Distribution of maximum total (blue) and dynamic (red) normal vertical stresses along the upstream face of monolith 14 – Imperial Valley earthquake – cases [-H] and [-H-V]

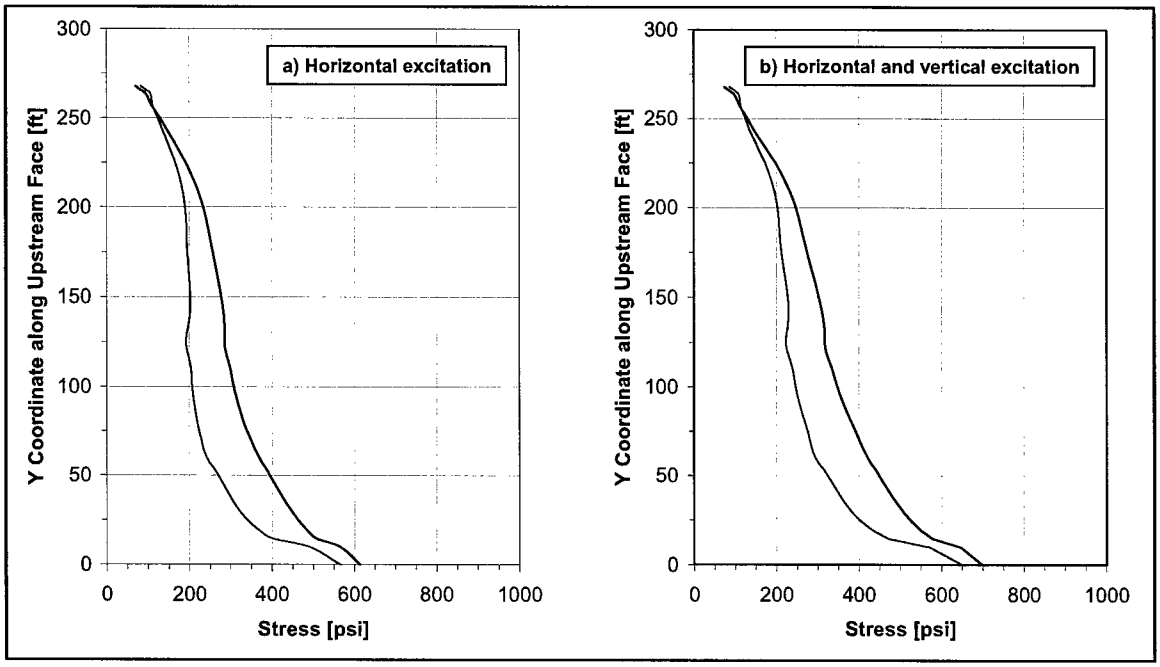

Figure 47. Distribution of maximum total (blue) and dynamic (red) normal vertical stresses along the upstream face of monolith 14 – Chalfant earthquake – cases [+H] and [+H+V]

those corresponding to both components considered simultaneously. Figure 47 shows the results corresponding to the Chalfant earthquake, with peak values of S_y = 650 psi and S_y^d = 699 psi (both ground motion components). For this particular case, the peak stresses corresponding to the horizontal excitation acting alone are slightly less than 90 percent (S_y^H = 613 psi and S_y^{Hd} = 565 psi) of those computed considering both earthquake components.

Comparison with simplified response spectrum analyses

A main objective of this study is to compare the results obtained by time history analysis with the maximum response estimates previously determined by SPK using a simplified response spectrum approach. Figures 48 and 49 show the variation of dynamic vertical stresses along the upstream faces of monolith 21 and 14, respectively. The black curve in those figures represents the maximum dynamic stress profile determined by the simplified response spectrum approach considering both components of the excitation. These results correspond to the middle section of monolith 21 (Figure 48) and to a sectional cut at a distance of 18.75 ft from the center of monolith 14 (Figure 49). The red curve represents the peak values of the dynamic stresses obtained by time history analysis. The time history results for monolith 21 (Figure 48) were obtained considering both components of the Imperial Valley earthquake (combination [-H-V]). The time history results for monolith 14 (Figure 49) were obtained considering both components of the San Fernando earthquake (combination [+H-V]). The stress results for monolith 21

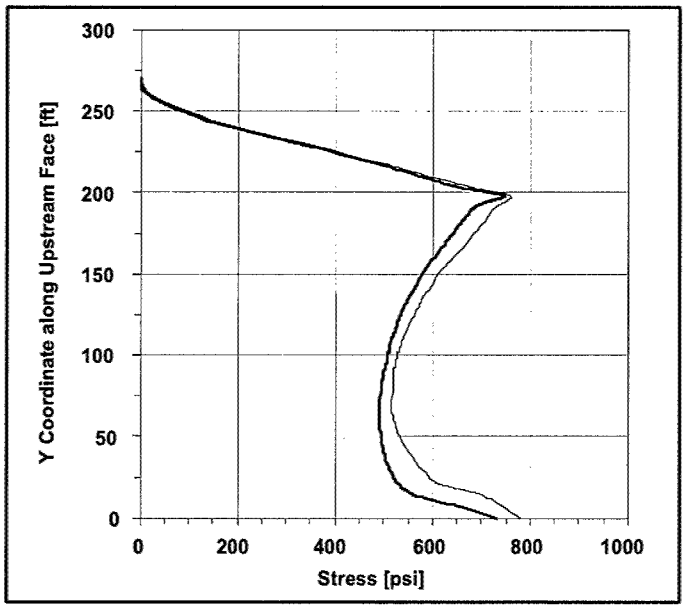

Figure 48. Comparison of maximum values of dynamic normal vertical stresses along the upstream face of monolith 21 obtained by simplified response spectrum analysis (black) and time-history analysis (red)

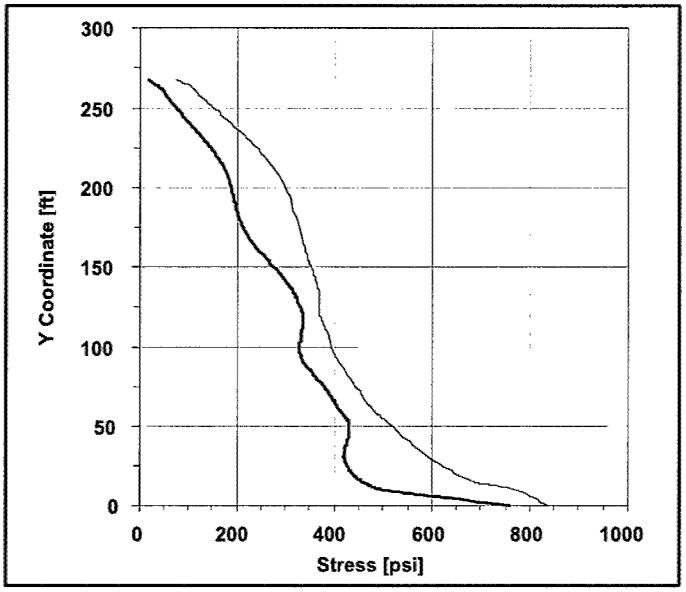

Figure 49. Comparison of maximum values of dynamic normal vertical stresses along the upstream face of monolith 14 obtained by simplified response spectrum analysis (black) and time-history analysis (red)

show good agreement along the height, and the stress values obtained by time history analysis are slightly higher than those predicted by the simplified response spectrum approach. The results for monolith 14, however, show larger differences between the maximum values predicted by the two approaches. For this case, the peak stress values obtained by time history analysis are higher than those calculated using the simplified response spectrum approach. It is important to consider the fundamental difference between the two underlying finite element models. The time history analysis is based on a 2D model that incorporates the influence of the spillway pier and the chamber and conduit voids in an approximate manner (using equivalent material properties), whereas the simplified response spectrum analysis is based on a 3D representation of the geometry. This is very relevant because the time history results directly reflect the influence of the equivalent representation of the spillway pier at the top of the model, while the results from the simplified response spectrum approach correspond to a sectional cut at 18.75 ft from the center of the monolith, not directly below the spillway pier.

Figure 50 shows the variation of maximum dynamic vertical stresses along the width of monolith 14 for two different elevations. The two elevations are 209.4 and 277.4 ft, and they correspond to the upper and lower conduit soffits, respectively. The black curves represent the stress distribution predicted by the simplified response spectrum approach based on a 3D model of the monolith. The stress increase induced by the presence of the conduit openings is quite noticeable. The peak values of dynamic vertical stresses at those elevations obtained by time history analysis are also shown in the figure, and they were obtained considering both components of the San Fernando earthquake (combination [+H-V]). These results were determined based on a 2D model and they are represented as constant values across the width of the section. In both cases, the peak values obtained by time history analysis are bracketed by the values determined by the simplified response spectrum approach across the section width.

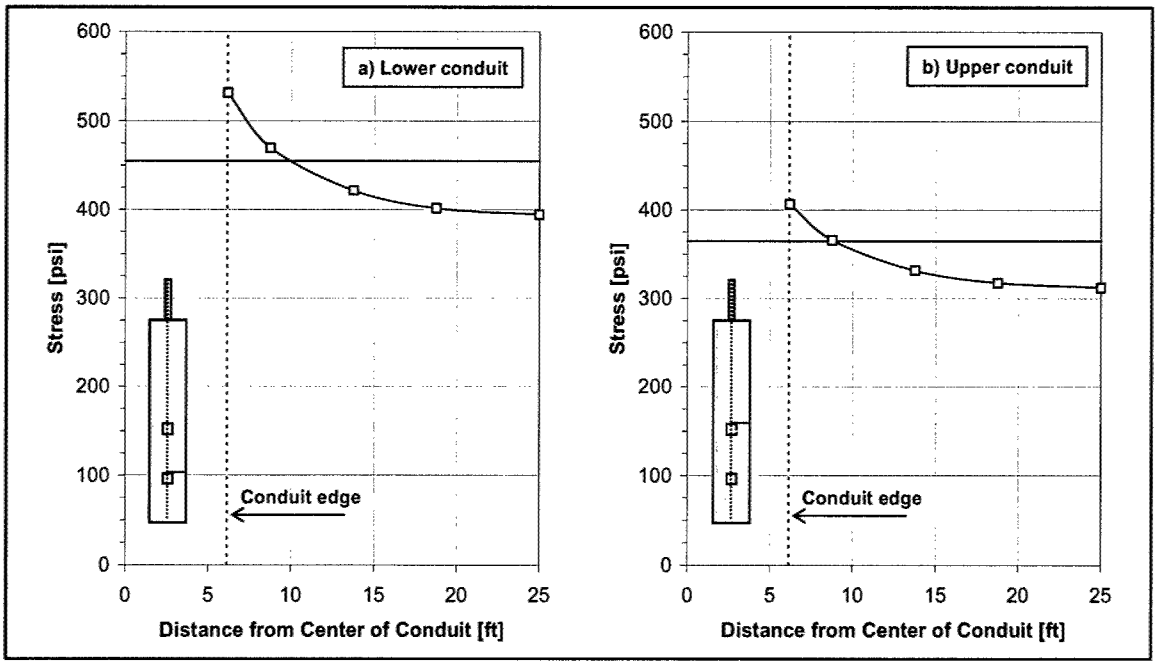

Figure 50. Maximum dynamic normal vertical stresses along the width of the upstream face of monolith 14 obtained by simplified response spectrum analysis (black) and time-history analysis (red)

4 Conclusions

This report presents a series of finite-element based dynamic stress analyses performed on monoliths 14 and 21 of Folsom Dam. The linear time-history response analyses were performed using the computer program EAGD-84 as the analysis platform. The corresponding formulation accounts for dam-foundation interaction and water compressibility effects, and this is entirely consistent with the previous seismic studies performed by the Sacramento District using Chopra's simplified analysis procedure. The middle cross sections of the monoliths were idealized by two-dimensional finite-element models consisting of four-node quadrilateral elements.

The time-history response analyses were performed using three sets of input motions spectrally matched to the adopted MCE horizontal and vertical spectra. It is interesting to note that in general these three input motions generated quantitatively and qualitatively similar results because of the excellent spectral matching of the input time histories used in the linear analyses. In all cases, the critical loading scenario corresponded to a case in which the base excitation consisted of a combination of both horizontal and vertical input motion components.

These two-dimensional analyses identified three critical regions in the nonoverflow monolith analyzed (monolith 21): the upstream dam-foundation contact corner (heel), as well as the regions along both upstream and downstream faces located at about 72 percent of the height of the monolith. The reported principal stresses reached a peak value of about 760 psi for the San Fernando earthquake. It must be mentioned that this value is representative of a finite area in the critical region that is characterized by the smallest contributing element. In the case of a corner point, such as the heel, there could be significant stress concentrations induced by the geometry of the section and any imposed boundary conditions. In this case, the determination of the peak stress value will be drastically affected by the local density of the finite-element mesh. Therefore, it is of paramount importance to evaluate not only the peak value but also the corresponding local stress gradient. Careful engineering judgment should be considered when evaluating these types of stress concentration effects. In all cases, the high tensile stress values were confined to limited regions in the neighborhood of the critical locations. The corresponding stress time histories indicated that critical tensile demands occurred at very isolated instances along the duration of the earthquake.

The analyses performed on the two-dimensional overflow section (monolith 14) identified the heel as the critical region, where peak principal stresses reached a value of about 897 psi, also for the San Fernando earthquake. No other critical areas were identified based on the type of finite-element model used for these studies. Additional investigations of stress concentration effects induced in the perimeter of the chambers and the conduits would require the three-dimensional modeling of the monolith geometry. As previously indicated, the tensile demands must be evaluated not only as isolated peak values but also considering their temporal variation and the corresponding spatial gradient. The stress time history at the critical location indicated a few isolated excursions above an assumed strength threshold (700 psi), and in all cases the areas of excessive tensile demands were limited to the region immediately near the heel.

All compressive stresses predicted by these analyses are well below the corresponding strength limit. The levels of tensile demands predicted by this study indicate that localized damage in the form of tensile cracking is likely to take place in limited areas of monoliths 14 and 21 when subjected to extreme seismic loading, but this is still acceptable seismic performance under MCE conditions.

References

Chopra, A. K. (1978). "Earthquake resistant design of concrete gravity dams," *Journal of the Structural Division*, ASCE 104(ST6), 953-971.

Chopra, A.K., and Hanchen, T. (1989). "Simplified earthquake analysis of gated spillway monoliths of concrete gravity dams," Technical Report SL-89-4, U.S. Army Engineer Waterways Experiment Station, Vicksburg, MS.

Fenves, G., and Chopra, A. K. (1984). "EAGD-84, A computer program for earthquake analysis of concrete gravity dams," Earthquake Engineering Research Center, Report No. UCB/EERC-84/11, University of California, Berkeley, CA.

_____. (1986). "Simplified analysis for earthquake resistant design of concrete gravity dams," Report No. UCB/EERC-85/10, Earthquake Engineering Research Center, University of California, Berkeley.

GT STRUDL. "Structural design and analysis software," CASE Center, School of Civil and Environmental Engineering, Georgia Institute of Technology, Atlanta, GA.

Hall, R. L., Woodson, S. C., and Nau, J. M. (1989). "Seismic stability evaluation of Folsom Dam and reservoir project; Report 3, Concrete gravity dam," Technical Report GL-87-14, U.S. Army Engineer Waterways Experiment Station, Vicksburg, MS.

Headquarters, U.S. Army Corps of Engineers. (1995). "Gravity dam design," Engineer Manual 1110-2-2200, Washington, DC.

_____. (1999). "Response spectra and seismic analysis for concrete hydraulic structures," Engineer Manual 1110-2-6050, Washington, DC.

URS Corporation. (2001). "Deterministic and probabilistic seismic hazard analyses – Folsom Dam – Central California," Final Report, Oakland, CA.

_____. (2002). "Deterministic and probabilistic seismic hazard analyses – Folsom Dam – Central California," Supplemental Report, Oakland, CA.

URS Corporation. (2003). "Deterministic and probabilistic seismic hazard analyses – Folsom Dam – Central California," Supplemental Report II, Oakland, CA.

Wong, C., Poeppelman, R., and Graff, S. (2002). "Preliminary earthquake response analysis of Folsom Dam spillway monoliths," Proceedings, 3rd U.S.-Japan Workshop on Advanced Research on Earthquake Engineering for Dams, June 22-23, San Diego, CA.

REPORT DOCUMENTATION PAGE

Form Approved
OMB No. 0704-0188

1. REPORT DATE *(DD-MM-YYYY)*	2. REPORT TYPE	3. DATES COVERED *(From - To)*
September 2004	Final report	

4. TITLE AND SUBTITLE

Folsom Dam Outlet Works Modification Project: Dynamic Stress Analysis of Overflow and Nonoverflow Sections

5a. CONTRACT NUMBER

5b. GRANT NUMBER

5c. PROGRAM ELEMENT NUMBER

6. AUTHOR(S)

Enrique E. Matheu, Robert L. Hall, and Raju V. Kala

5d. PROJECT NUMBER

5e. TASK NUMBER

5f. WORK UNIT NUMBER
33013

7. PERFORMING ORGANIZATION NAME(S) AND ADDRESS(ES)

Geotechnical and Structures Laboratory, U.S. Army Engineer Research and Development Center, 3909 Halls Ferry Road, Vicksburg, MS 39180-6199

8. PERFORMING ORGANIZATION REPORT NUMBER

ERDC/GSL TR-04-13

9. SPONSORING / MONITORING AGENCY NAME(S) AND ADDRESS(ES)

U.S. Army Corps of Engineers
Washington, DC 20314-1000

10. SPONSOR/MONITOR'S ACRONYM(S)

11. SPONSOR/MONITOR'S REPORT NUMBER(S)

12. DISTRIBUTION / AVAILABILITY STATEMENT

Approved for public release; distribution is unlimited.

13. SUPPLEMENTARY NOTES

14. ABSTRACT

This report summarizes the results corresponding to a series of dynamic stress analyses performed on an overflow and a nonoverflow monolith of Folsom Dam, California. The monoliths selected for analysis were monoliths 14 and 21, and they were chosen as representative of critical overflow and nonoverflow configurations. The analyses were conducted using the computer program EAGD-84, developed by Professor A. K. Chopra and co-workers at the University of California at Berkeley. The analyses accounted for dam-foundation interaction and water compressibility effects, and considered two loading scenarios: (a) horizontal component of the ground motion and (b) horizontal and vertical components of the ground motion. The results are reported in terms of the maximum expected stresses under extreme loading conditions (maximum credible earthquake, MCE), and they are compared with those results obtained from analyses performed by engineers at the Sacramento District using a response-spectrum-based procedure also developed by Professor Chopra. The influence of the vertical component of the ground motion on the magnitude and distribution of the dynamic stresses is investigated. The levels of tensile demands predicted by this study indicate that localized damage in the form of tensile cracking is likely to take place in limited areas of monoliths 14 and 21 when subjected to extreme seismic loading, but this is still acceptable seismic performance under MCE conditions.

15. SUBJECT TERMS

Concrete dams	Dynamic stresses	Nonoverflow monolith
Dynamic stress analysis	Ground motions	Overflow monolith

16. SECURITY CLASSIFICATION OF:			17. LIMITATION OF ABSTRACT	18. NUMBER OF PAGES	19a. NAME OF RESPONSIBLE PERSON Enrique E. Matheu
a. REPORT	b. ABSTRACT	c. THIS PAGE			19b. TELEPHONE NUMBER *(include area code)*
UNCLASSIFIED	UNCLASSIFIED	UNCLASSIFIED		64	(601) 634-3235

Standard Form 298 (Rev. 8-98)
Prescribed by ANSI Std. 239.18